Influence of Protein Environment on Tryptophan Fluorescence

Andrew W. McMillan

A dissertation

submitted in partial fulfillment of

the requirements for the degree of

Doctor of Philosophy

University of Washington

2012

Reading Committee:

William Parson, Chair

Niels Andersen

Ron Stenkamp

Program Authorized to Offer Degree:

Biochemistry

University of Washington

Abstract

Influence of Protein Environment on Tryptophan Fluorescence

Andrew W. McMillan

Chair of Supervisory Committee:

Professor William Parson

Biochemistry

Tryptophan fluorescence is often used as a probe of protein structure. One example of this involved the study how a mutation in catechol O-methyltrasferase produces a less stable protein. Other examples of the use of tryptophan and what factors influence variations in emission energy and quantum yield are discussed. Further investigation of these factors was carried out using two simple peptide systems, followed by mixed molecular dynamics/quantum mechanics simulations to calculate the energetics of quenching by electron transfer. These simulations used a simple quantum model that allowed tight coupling between classical and quantum calculations. It also incorporates potentials from induced dipoles. These simulations resulted in a correlation of quantum yield and charge-transfer energies. Interactions between the charge acceptor and protein stabilized charge in one system, while the other was stabilized by interactions between water and both the charge donor and acceptor.

TABLE OF CONTENTS

LIST OF FIGURES

LIST OF TABLES

Introduction

Tryptophan fluorescence can be a very useful tool for probing protein structure because the emission energy and the quantum yield are both very sensitive to the surroundings. Quantum yields have been reported as low as 0.01 and as high as 0.31, and emission peaks have been seen ranging from 360 nm for 3-methylindole to the extremely blue-shifted fluorescence of azurin near 300 nm. As a natural amino acid, tryptophan can often be easily introduced into a protein if it is not already present, and is rare enough that fluorescence can often be attributed to a particular position in the protein. Fluorescence can be measured at lower concentrations or under conditions where other methods may be less feasible.

Despite these useful properties, fluorescence is still commonly treated largely as a qualitative property. The sensitivity to the surroundings that makes it a useful probe can also cause difficulties due to the variety of complex factors that influence the fluorescence of a protein. Theoretical explanations are further complicated by the presence of two excited states (referred to as ^1L_a and ^1L_b) that can both contribute to emission and have similar energy levels. While fluorescent properties of some proteins can be attributed to specific influences, systematic investigations have met with mixed explanatory power. In particular, the influences of the surroundings on quantum yield are still poorly understood.

To investigate this area I have taken advantage of the availability of two simplified model peptides, one a β-hairpin, the other a variant of the Trp-cage mini-protein. Both of these systems have high thermodynamic stability, making them amenable to changes at specific positions. By making changes near a single tryptophan, while leaving the rest of the protein unaltered, one can identify specific changes that affect fluorescence emission. Some of these results can be further

interpreted through the use of mixed Molecular Dynamics-Quantum Mechanics (MD-QM) simulations. The particular implementation of MD-QM I used has incorporated a thorough treatment of polarization of atoms and a tight connection between classical and quantum properties. These improvements will hopefully give further insight into the mechanisms that are responsible for variations of fluorescence seen experimentally and will aid in interpretation of these results.

Chapter 1: Catechol O-Methyltransferase

My interest in tryptophan fluorescence grew out of studies of catechol O-methyltransferase (COMT). This enzyme catalyzes the transfer of methyl groups from S-adenosyl-methionine (SAM) to a variety of catechols, notably including catecholamine neurotransmitters such as dopamine and epinephrine and catechol estrogens. COMT exists as two isoforms produced from alternative start codons. The longer transcript produces a protein (MB-COMT) with an additional 50 amino acids that form a transmembrane helix anchoring COMT to the endoplasmic reticulum membrane while the smaller protein (S-COMT) remains soluble.[1] These two isoforms have different substrate specificies[2] and tissue distributions.[3]

Effects of 108V/M polymorphism:

COMT is notable for having a polymorphism at position 108 in the soluble form of the protein, or position 158 in the membrane bound form. Residue 108 (colored cyan in figure 1) is valine in most people, as well as in all non-human primates. However a methionine at this position is common in some human populations, making up approximately half the gene pool among Caucasians.[4] Although purfied 108V and 108M protein have similar kinetic properties, individuals with the 108M genotype have lower levels of COMT in their blood, and the protein produced by these individuals has a shorter half-life.[2] The resulting differences in enzymatic activity in the body appear to have several impacts on health.

Schizophrenia:

Links between COMT genotype and the risk of schizophrenia have been somewhat mixed, though a haplotype with the 108V allele and two other polymorphic alleles has been

associated with an increased risk of schizophrenia.[5,6] On the other hand, the 108M allele has been associated with more violent forms of schizophrenia. This allele was also found to be more common among individuals requiring a higher dosage of anti-psychotic medication.[7] Administering SAM to schizophrenic patients was reported to decrease aggressiveness and lowered dopamine and noradrenaline levels.[8]

Other Mental Disorders:

Several studies have found an association between the 108M allele and individuals with rapid-cycling bipolar disorder.[9] This allele has also been associated with obsessive-compulsive disorder,[10] adult onset alcoholism,[11] and attention deficit disorder.[12] COMT activity also has an impact on Parkinsonism by acting on both dopamine[13] and L-dopa, which is administered as a treatment.[14]

Effects on Normal Mental Function:

The increased amount of active neurotransmitters in the brain as a result of decreased COMT activity has been suggested to have effects on mental function in more subtle ways than the previously described mental disorders. Dopamine plays a role in reward seeking and the valine allele of COMT has been reported to slow response time in evaluating possible rewards.[15,16]

The methionine allele has been associated with better working memory both in normal individuals and in individuals with schizophrenia.[17–19] COMT knockout mice also show increased memory, but greater stress response and pain sensitivity.[20,21] The 108M allele was associated with inhibition of a startle response.[22] COMT has also been implicated in more long-term effects, where the 108M allele was associated with a larger hippocampus volume.[23]

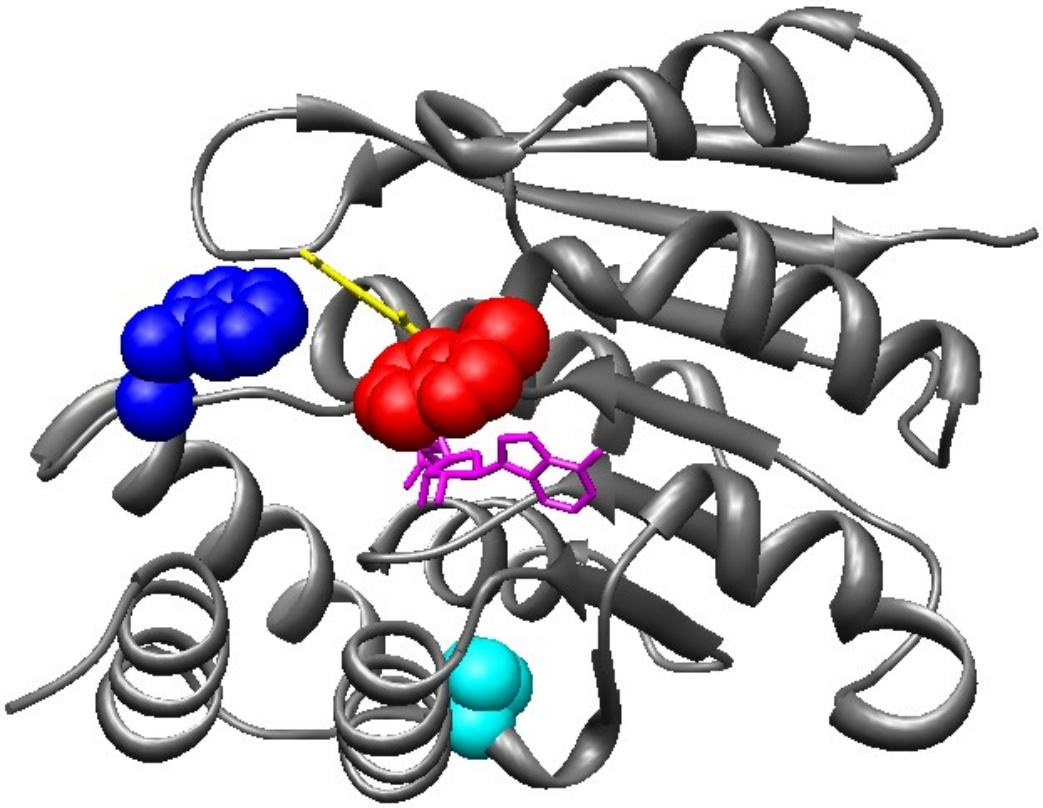

Figure 1: Structure of Catechol O-Methyltransferase Crystal Structure of 108V S-COMT. Tryptophan residues 38 (blue), and 143 (red) and valine 108 (cyan) are shown as space filling models. The substrates SAM (magenta) and dinitrocatechol (yellow) are shown as balls and sticks.[24]

Biophysical characterization:

The lower levels of COMT found in individuals with the methionine allele could be explained by either lower production or faster turnover. Nackley et al. that found a haplotype associated with the V108M mutation favors the formation of an mRNA hairpin upstream of the translation start site,[25] resulting in less protein being produced. On the other hand, others have reported differences in stability and turnover directly in the protein.[2] My lab found the 108M variant to be less stable as measured by circular dichroism[26] (figure 2) and dynamic light scattering.[26] Molecular dynamics simulations predicted changes in sidechain packing and a wider range of conformations[27]

My contribution was to study the differences between 108V and 108M protein that could be seen with tryptophan fluorescence. COMT contains two tryptophan residues, both found near the enzyme's active site when SAM is bound,[24] (figure 1) though later work found Trp38 further away in the apo-protein.[28] When substrate is bound, W143 interacts closely with the adenosine ring of SAM, while W38 interacts with the catechol.[24,28] The fluorescence of these two tryptophans can serve as probes of how changing valine to methionine alters the structure away from the mutation site. Each tryptophan's contribution to fluorescence was determined by creating single-tryptophan mutants with the other residue changed to tyrosine.

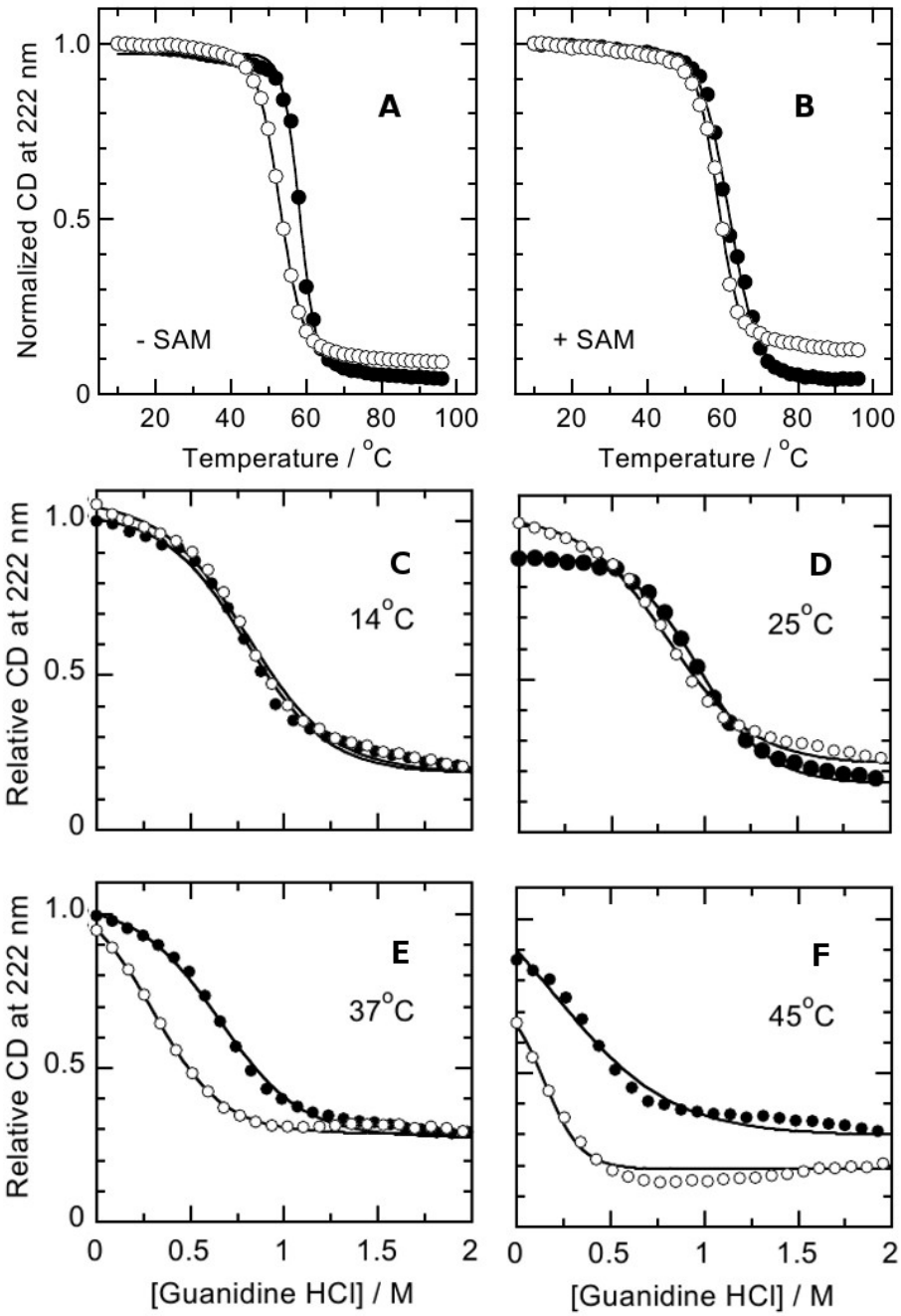

Figure 2: Circular Dichroism of COMT at 222 nm In all panels, open circles are 108M; filled circles are 108V. (A) Thermal denaturation in the absence of SAM, (B) Thermal denaturation in the presence of SAM. (C-F) Chemical denaturation by guanidinium hydrochloride at the indicated temperatures.[26]

Methods*:*

(This section is partially reproduced from Rutherford et al. 2008.[26])

Protein expression:

108V or 108M S-COMT were expressed from plasmids that provided a C-terminal $(His)_6$ tag preceded by a thrombin cleavage site (LeuValProArgGlySer). W38F, and W143F mutants were generated with the QuickChange® site-directed mutagenesis kit (Stratagene, La Jolla, CA), and were confirmed by DNA sequencing. Protein was expressed in BL21 *Escherichia coli* cells induced by isopropylthiogalactoside. Collected cells were lysed by sonication and centrifuged for 30 min. at 12000 × g and 4 °C. The supernatant was filtered through 0.22 μm pores and added to a TALON metal affinity column from Invitrogen. Non-specifically bound proteins were removed by successive washes with 50 mM Na_2HPO_4 (pH 7.5), 300 mM NaCl, 2 mM $MgCl_2$ and 7 mM β-mercaptoethanol containing 0 and 7 mM imidazole. COMT was then eluted with 400 mM imidazole and dialyzed overnight in 50 mM Na_2HPO_4 (pH 7.5), 250 mM NaCl, 2 mM $MgCl_2$ and 5 mM dithiothreitol (DTT). The protein was further purified by size exclusion chromatography using a XK-16/100 Superdex 75 preparation-grade chromatography column (Amersham Biosciences, Piscat- away, NJ) in the same buffer. Final protein concentration was determined using the Bradfrod assay. The purified protein was then stored at -20°C in aliquots to be used for fluorescence measurements at a later time.

Fluorescence Measurements:

Fluorescence was measured with a Perkin-Elmer LS-50B fluorescence spectrometer equipped with a thermostated cell holder (Perkin-Elmer, Norwalk, CT). The samples contained

0.16±0.02 μM S-COMT in the assay buffer of 50 mM Na_2HPO_4 (pH 7), 200 mM NaCl, 2 mM $MgCl_2$ and 2 mM DTT.

The excitation wavelength was 280 nm and emission spectra were recorded between 310 and 400 nm with excitation and detection bandpasses of 10 nm, except for measurements to determine absolute quantum yield. These spectra used an excitation wavelength of 295 nm and integrated the corrected emission spectra from 305 to 450 nm. Raman scattering by the solvent was subtracted, and the wavelength dependence of the detection efficiency was corrected for by using tyrosine, tryptophan, and fluorescein as standards. The tryptophan emission maximum (λ_{max}) was obtained by fitting the corrected emission spectrum between 330 and 395 nm with a Gaussian function on a wavenumber scale.

To study thermal unfolding, the buffer was equilibrated at the desired temperature, COMT was added, and the emission spectrum was recorded within one minute so that the time-dependent decay of the fluorescence was negligible. To study chemical unfolding, aliquots of a concentrated guanidinium hydrochloride (GuHCl) solution were added to a thermally equilibrated solution of COMT. Identical aliquots of standard buffer without GuHCl were added to a reference solution of COMT. The sample fluorescence intensities were divided by the corresponding reference intensities to correct for protein dilution and the small time-dependent decrease of fluorescence. A similar process was used for the addition of acrylamide for quenching experiments. The absolute fluorescence yield of 108V S-COMT was measured by comparison with tryptophan in water, which has a fluorescence yield of 0.13.[29,30].

Transition midpoints for either chemical or thermal unfolding were estimated by fitting the fluorescence (F) by nonlinear least-squares with the expression

$$F = F_0 + F_1/(1 + exp(\frac{x_{mid} - x}{x_0})) \quad \text{(Equation 1)}$$

where x is either temperature or guanidinium hydrochloride concentration, x_{mid} is the transition midpoint (T_m or $C_{1/2}$), and F_0, F_1 and x_0 are free parameters. This makes the simplifying assumptions that the change in F occurs in a single transition and that the slopes of the baselines below and above the transition are zero. To analyze the dependence of the fluorescence amplitude on temperature (T) more closely, we fit the values of 1/F between 10 and 26 °C (28 °C in the presence of SAM) with a second-order polynomial:

$$F(T) = C_0 + C_1 * T + C_2 * T^2 \quad \text{(Equation 2)}$$

The additional decrease in fluorescence at higher temperatures (ΔF) then was extracted by plotting the function

$$\Delta F = F(T) - [C_0 + C_1 * T + C_2 * T^2]^{-1} \quad \text{(Equation 3)}$$

This assumes that the quenching processes that occur at low temperatures continue with the same temperature dependence when the protein structure changes at higher temperatures. The free energy of unfolding in the absence of GuHCl ($\Delta G°_{UN}$) was calculated by the linear-extrapolation method, which takes the slopes of the baselines into account. In this procedure, the fluorescence signal (S) is fit by the expression

$$S = (S_N + m_N[D]) + (S_U + m_U[D])\frac{exp(-\frac{\Delta G^\circ_{UN} + m_G[D]}{RT})}{(1 + exp(-\frac{\Delta G^\circ_{UN} + m_G[D]}{RT})} \quad \text{(Equation 4)}$$

where S_N and S_U are the intercepts and m_N and m_U the slopes (dS/d[D]) of the pre- and post-unfolding baselines, respectively, [D] is the GuHCl concentration, and m_G is the linear dependence on [D] of the free energy of unfolding. An estimate of m_G was obtained by the

expression $m_G \approx [0.859 + 2.2 \times 10{-}4 \times \Delta ASA] \approx [0.859 + 2.2 \times 10{-}4 \times (93 \times N_{res} - 907)] = 5.18$ kcal·mol− 1 ·M− 1, where ΔASA is the increase in solvent-accessible surface area upon unfolding (in units of $Å^2$) and N_{res} is the number of residues in the protein (221, not including the polyhistidine tag).

For acrylamide quenching, data were fit to the Stern-Volmer equation

$$F_0/F_Q = K_{SV}[Q] + 1 \qquad \text{(Equation 5)}$$

where F_0 is the area of the fluorescence emission spectrum without acrylamide, F_Q is the area at the acrylamide concentration of [Q], and K_{SV} is the Stern-Volmer constant. Making the assumption that quantum yield and fluorescence lifetime are proportional, K_{SV} can be divided by the quantum yield to obtain a bimolecular quenching rate constant k_q.

Fluorescence Results

Emission Spectra of Double and Single Trp Proteins:

Figure 3A and B show the emission spectra of 108V and 108M S-COMT and the tryptophan mutants at 14°C. 108V and 108M S-COMT have very similar spectra, with a peak intensity at 345 ± 1 and 344 ± 1 nm for 108V and 108M, respectively and 108M having a slightly higher quantum yield. The sum of the two single Trp mutants' spectra (dotted line in figure 3) tracked the double-Trp spectra closely at longer wavelengths, and diverged only at the shorter wavelengths where tyrosine contributes to the emission, suggesting that the remaining tryptophan is not perturbed. Both of the W38Y mutants (red lines in figure 3) have red-shifted spectra by about 2 nm compared to the wildtype proteins, while the W143Y mutant spectra (blue lines in figure 3) are blue-shifted by 8 nm. The W38Y proteins have about twice the intensity of

the W143Y mutants.

Fluorescence As a Probe of Thermal Unfolding:

All of the proteins showed decreases in fluorescence and shifts in emission peak at increased temperatures (figure 4). The single-tryptophan mutants have a broader transition that occurs at lower temperatures, suggesting the mutations destabilize the protein somewhat (figure 5A and B). However with both double- and single-tryptophans proteins, 108M S-COMT undergoes the melting transition at a lower temperature than 108V S-COMT (Table 1). This is consistent with the earlier circular dichroism measurements and supports the idea that 108M S-COMT is intrinsically less stable. In the presence of SAM, the stability of 108M S-COMT becomes similar to that of 108V COMT.

Fluorescence As a Probe of Chemical Unfolding

Figures 5C-F and 6 show the change in fluorescence upon the addition of guanidinium hydrochloride (GuHCl) for the wildtype and single-tryptophan proteins. As with thermal unfolding, the fluorescence of the double tryptophan proteins decreases and shifts to the red upon unfolding by GuHCl, and the 108M proteins are more sensitive to GuHCl than the 108V variants. The two single-tryptophan mutants show different responses, with the W38Y mutant having a large decrease in fluorescence intensity and a shift to a shorter wavelengths, while the W143Y mutant had a small change in intensity and a shift to longer wavelengths. The final emission energies did not converge to the same value, suggesting the protein may have some residual structure that provides different environments to the two tryptophans even at high GuHCl concentrations. The single tryptophan mutants also showed more sensitivity in 108M proteins than in 108V, like with the temperature experiments. .

The unfolding of S-COMT by GuHCl was reversible at 14°C and 25°C, allowing calculation of ΔG° for unfolding. At 14° C the wildtype tryptophan protein had a ΔG° of 5.23± 0.06 kcal/mol for 108V COMT and 4.81 ± 0.03 kcal/mol for 108M COMT. This decreased to 4.37± 0.02 kcal/mol in 108V COMT and 3.98 ± 0.04 kcal/mol for 108M COMT at 25°C. The single-tryptophan mutants unfold with a smaller ΔG°, but still showed a less stable protein for 108M by nearly the same amount (Table 1).

Acrylamide Quenching of Fluorescence:

Acrylamide can be used to monitor the solvent accessibility of a tryptophan residue, as it can quench fluorescence but only if acrylamide is able to directly make contact with the tryptophan. Figures 7A and B show the fitted Stern-Volmer plots for 108V and 108M COMT, respectively. Figure 7D shows the calculated quenching constant from these plots as a function of temperature. While the two proteins have similar quenching constants at low temperature, the quenching constants diverge as the temperature is increased. At 37°C, 108M S-COMT has a level of quenching that 108V S-COMT reaches only at 45°C. This result is consistent with the computer simulations showing the behavior of 108M S-COMT at 37°C is comparable to that of 108V S-COMT at a higher temperature.[27] Quenching experiments were also done with the 108V single-tryptophan mutants (figure 7C). These showed that the W143Y had less response to acrylamide compared to W38Y. This is consistent with the observation that the fluorescence of W38Y mutants undergoes larger changes in response to temperature or chemical denaturants.

Table 1: Fluorescence Properties of COMT with Wildtype Trp and Trp Mutants[26]

Property		**WT Trp**		**W38Y**		**W143Y**	
		108V	**108M**	**108V**	**108M**	**108V**	**108M**
Relative Quantum Yield		1.00	1.10	0.68	0.70	0.35	0.39
λ_{max} (nm)		345	344	347	346	337	336
$C_{1/2}$[a]	**14°C**	0.96±0.02	0.85±0.02	N/D[d]	N/D[d]	N/D[d]	N/D[d]
	25°C	0.79±0.02	0.71±0.02	0.65±0.02	0.46±0.02	0.72±0.02	0.71±0.02
$\Delta G°_{un}$[b]	**15°C**	5.23±0.06	4.81±0.03	N/D	N/D	N/D	N/D
	25°C	4.37±0.02	4.98±0.04	3.96±0.10	3.67±0.22	4.09±0.13	3.67±0.12
T_m[c]		44.9	38.4	ND[d]	ND[d]	ND[d]	ND[d]

[a] Molarity of guanidinim hydrochloride that decreases the fluorescence by ½
[b] ΔG of unfolding by guanidinim hydrochloride in units of kcal/mol
[c] Melting temperature
[d] ND = Not determined.

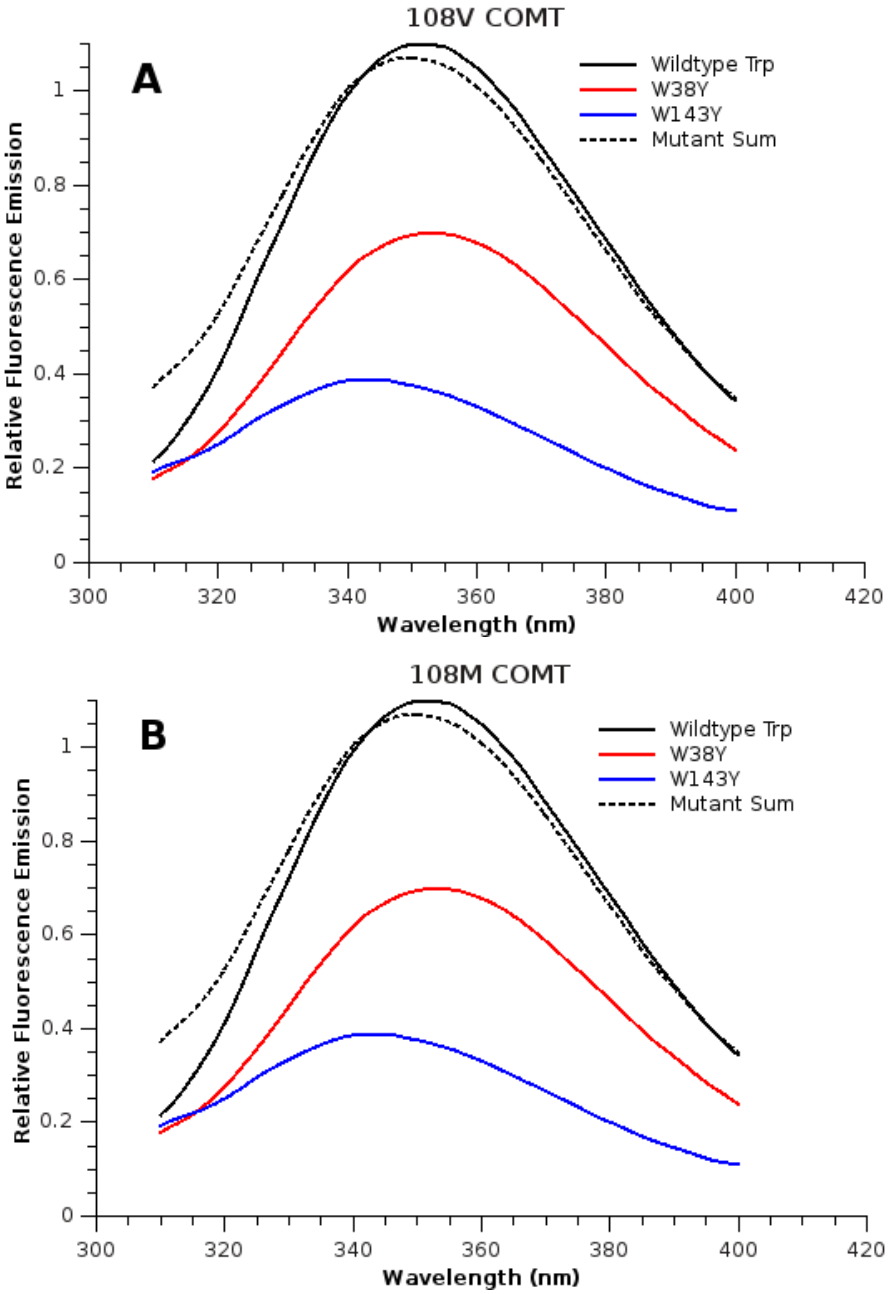

Figure 3: **COMT Emission spectra** Spectra of 108V (A) and 108M (B) COMT are shown for the wildtype and single tryptophan mutants. Also shown is the sum of the two tryptophan mutants.[26]

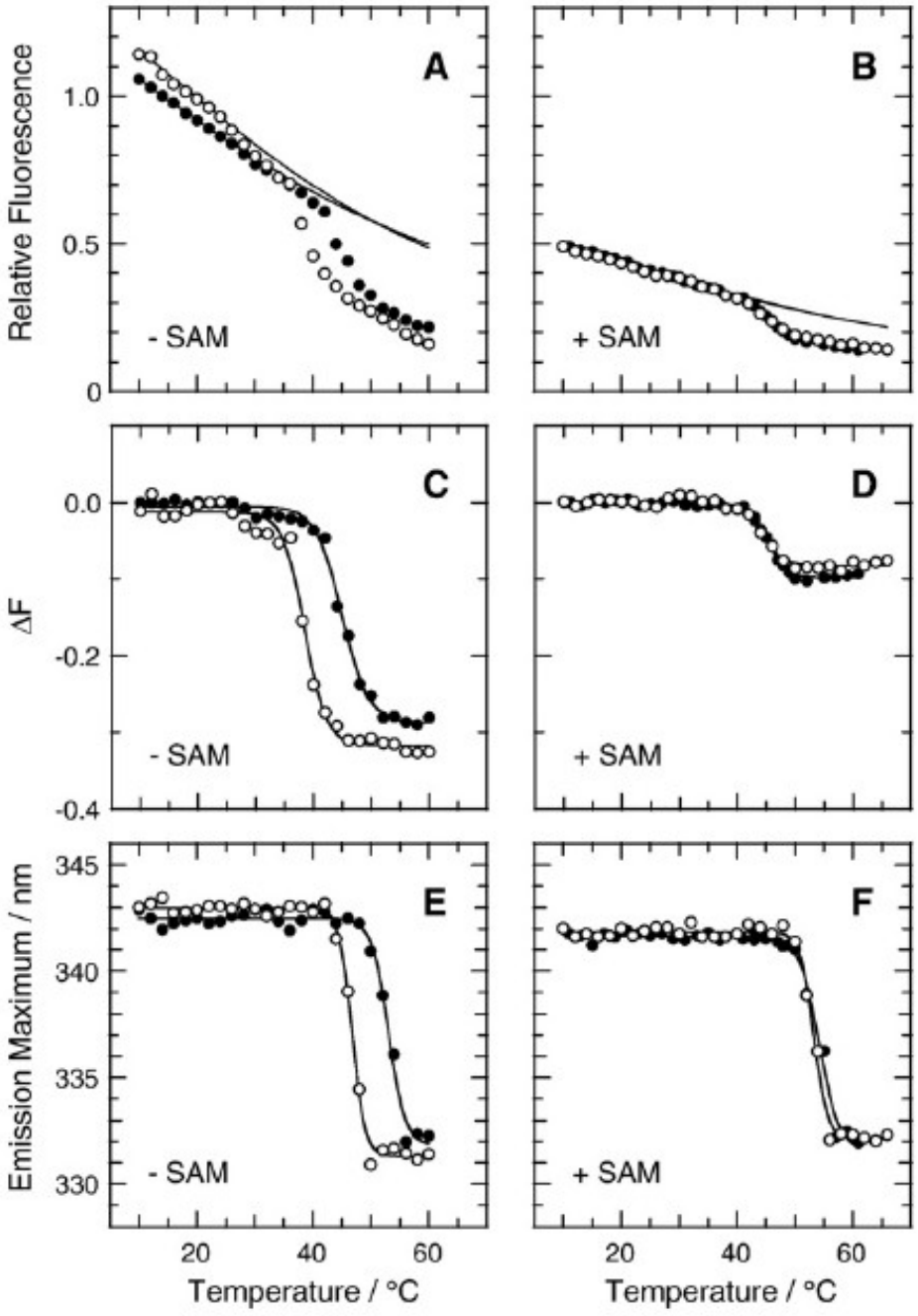

Figure 4 : Fluorescence emission as a function of temperature in the absence (A,C,E) and presence (B,D,F) of SAM. In all panels 108V are filled circles, and 108M are open circles. (A,B) Fluorescence intensity relative to 108V without SAM. Solid line is fit to points at low temperature as described in Equation 2 in the methods section. (C,D) Difference in energy from the predicted intensity based on the fitted curve. (E,F) Wavelength of Emission peak.[26]

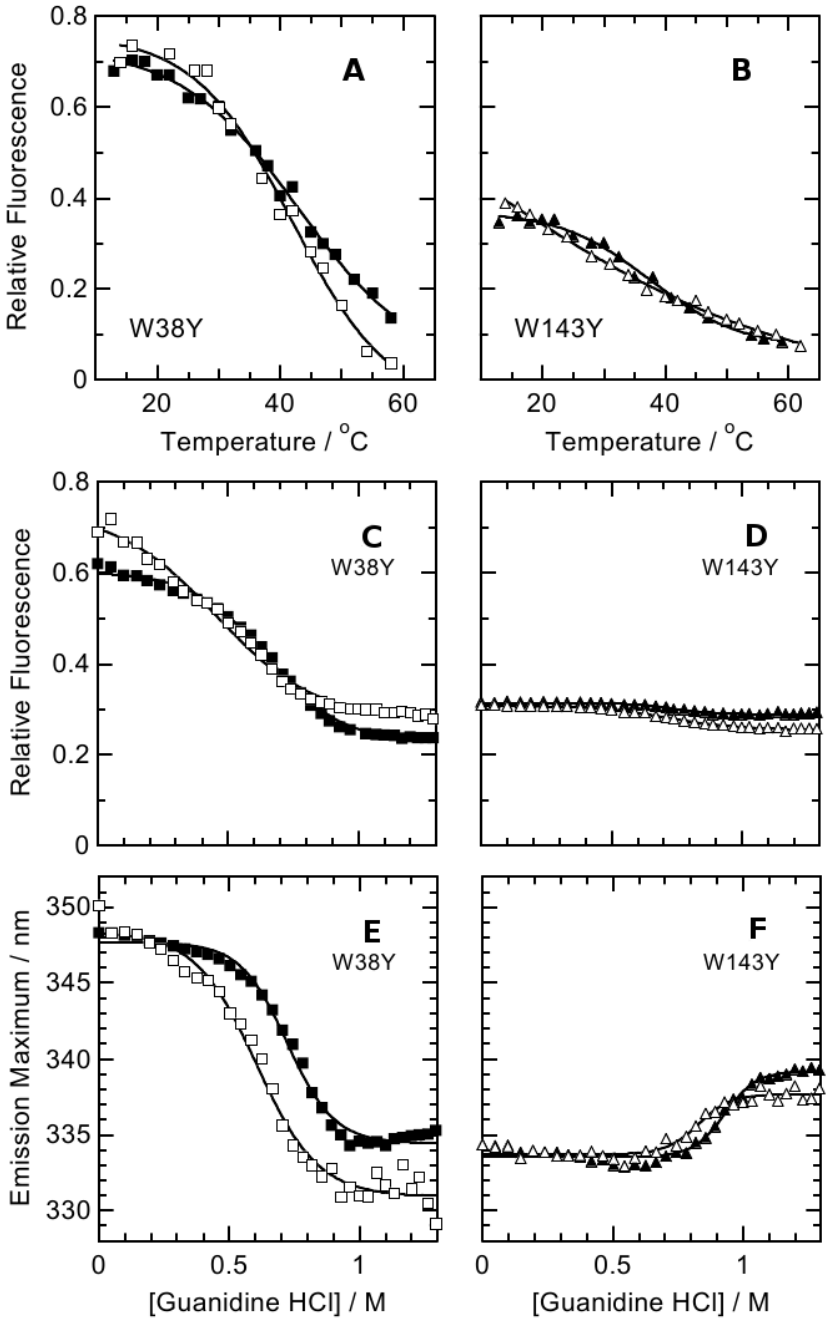

Figure 5: Fluorescence of single-tryptophan mutants upon unfolding. In all panels, solid markers indicate 108V COMT, open, 108M. (A,B) Fluorescence intensity as a function of temperature. (C,D) Fluorescence intensity as a function of guanidinium hydrochloride concentration. (E,F) Emission wavelength as a function of guanidinium hydrochloride concentration.[26]

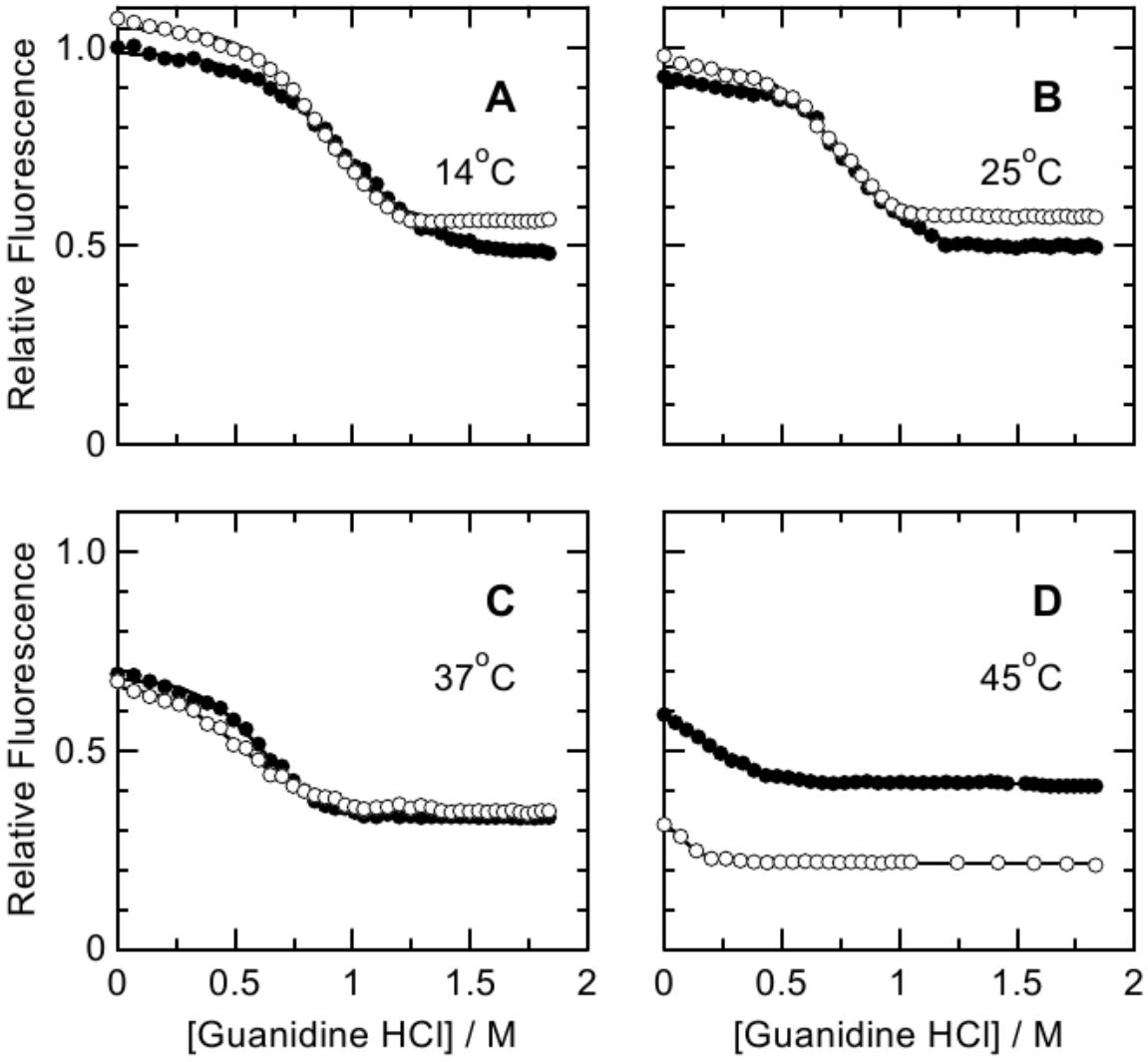

Figure 6: Unfolding of wildtype Trp S-COMT by guanidinium hydrochloride at different temperatures.[26] Solid circles show 108V, open circles show 108M.

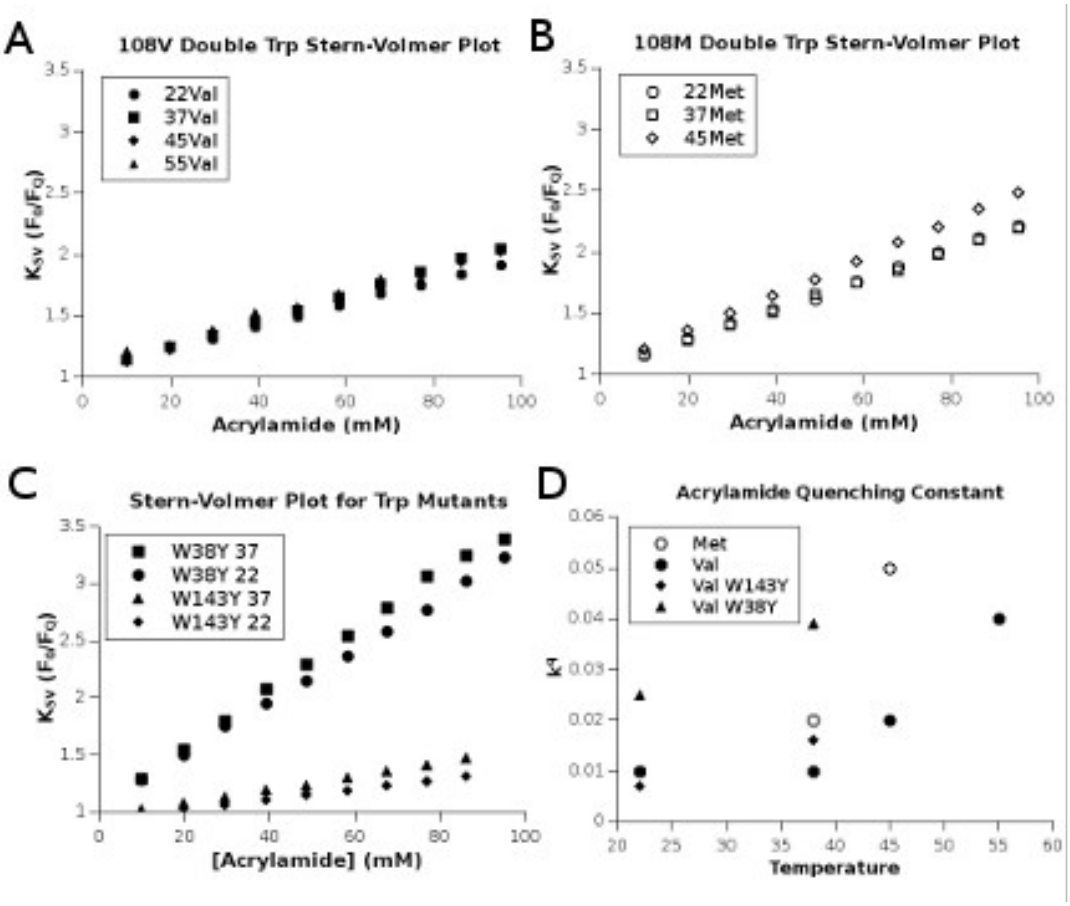

Figure 7: Quenching of COMT Fluorescence by acrylamide.Solid markers are all for 108V COMT, open markers for 108M. (A-C) Stern-Volmer plot of each system (D) bimolecular quenching rate constants at each temperature determined by dividing the fitted slope of (A-C) by the quantum yield.

Other COMT Isoforms

The experiments described so far all dealt with the smaller, soluble isoform of COMT. However many of the health impacts of 108V/M are related to mental function and the isoform found in the brain is the longer membrane-bound COMT. The additional 50 amino acids at the N-terminus of MB-COMT are predicted to form a single transmembrane helix along with a short linking loop with indeterminate structure. Bai et al. modeled this loop and predicted that these residues interact with the active site.[31] If this interaction is responsible for the different enzymatic properties of the two isoforms, only these extra residues might be needed to study these differences.

To investigate this, we obtained a plasmid containing the full-length protein from the Zhu lab, which was incorporated into the plasmid we had been using for S-COMT. We also created an intermediate, truncated form of COMT (T-COMT) that contained the same residues that were used in the model by Bai et al.,[31] plus the preceding glycine and an inserted methionine to act as a start codon (figure 8A).

While Bai et al. reported good expression of the full length MB-COMT as a soluble protein, it expressed poorly in our construct. However, the T-COMT construct expressed at comparable levels to S-COMT (figure 8B). This construct was used by undergraduates under my supervision to begin preliminary crystal screens and enzyme kinetics assays of T-COMT. While these did not lead to significant results, the high solubility of the T-COMT construct compared to MB-COMT suggests T-COMT deserves more investigation to confirm whether it could serve as an analog of the full-length isoform.

A)

```
MB-COMT  mpeapplla avllglvllv vllllrhwg wglcligwne filqpihnll mgdtkeqril
 T-COMT                                    mwne filqpihnll mgdtkeqril
 S-COMT                                                    mgdtkeqril
```

B)

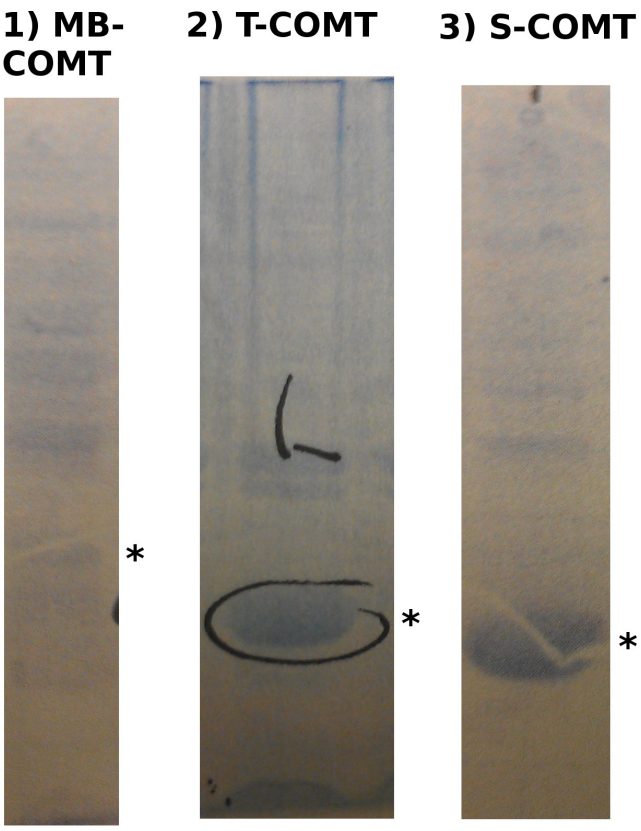

Figure 8:**COMT Isoform constructs** (A) Sequence of the N-terminus of COMT isoforms that were created. (B) Coomassie stained SDS-PAGE gel showing soluble fraction of MB-COMT(1), T-COMT (2) and S-COMT (3) protein expression. * indicates band of COMT protein. Proteins were seen more clearly on the original gels than in this photograph.

Discussion:

Tryptophan fluorescence complemented other methods to show 108M S-COMT is less stable than the 108V variant in the absence of SAM, and that the two proteins become more similar in the prescence of SAM. The changes in fluorescence were observed at lower temperature and denaturant conditions than the changes observed by circular dichroism. This suggests the fluorescence changes likely are due to smaller local changes rather than global unfolding of secondary structure, which CD would monitor. This is also consistent with other work showing COMT lost enzymatic activity at a temperature between the transitions measured by CD and fluorescence changes.[32] Loss of activity could require more denataturation than the local changes monitored by fluorescence, but less than complete unfolding.

While the single-Trp mutants were somewhat less stable than the wildtype proteins, the combined spectra at low temperature overlap with the wildtype spectra, so the general structures are likely to be very similar, at least in the region near the tryptophans. These two tryptophans occupy similar environments in the crystal structures of S-COMT with SAM bound, but had very different responses to unfolding. Understanding the cause of these differences could have provided some insight into how the 108V and 108M proteins differ and how methionine destabilizes the protein. The differences between fluorescence from Trp38 and Trp143 may have been less striking had if they were measured in the presence of SAM, since crystal structures with and without SAM show the loop containing Trp38 is very different positions.[28] Such measurements would be complicated by absorbance of the adenosine moity of SAM. Still, the different fluorescence properties of the two tryptophans without SAM illustrate how better understanding of tryptophan fluorescence could be useful.

Chapter 2: Tryptophan Fluorescence in Other Proteins and Other Model Compounds

Use of Tryptophan as a probe:

Tryptophan is widely used in other settings to study proteins. Steady-state fluorescence can be used to identify regions of a protein undergoing conformational changes.[33–36] and to monitor interaction with ligands or other proteins.[35,37–39] Because it is possible to monitor fluorescence in real time, it is va ery useful probe of dynamic behavior, such as ligand binding[38] or protein folding.[40–45]

While being able to measure fluorescence under conditions that are not amenable to other structural studies is useful,[26,35] it can be difficult to interpret such results. It would be useful to be able to attribute observed changes in fluorescence to a specific structural change. However understanding of tryptophan fluorescence is still somewhat rudimentary.

Functional significance of tryptophan photochemistry

While the fluorescence of tryptophan is often simply used as a tool to observe proteins, some proteins may make use of unusual tryptophan properties to carry out important functions. One example of this is γ-crystallin, one of the proteins that forms the lens of the eye in mammals. In addition to focusing light, the lens protects the retina by filtering out light between 295 and 400 nm. Serving this function could damage proteins forming the lens, and covalently damaged γ-crystallin has been associated with cataracts.[46] King and co-workers have proposed that electron transfer involving tryptophan can help protect these proteins, which must remain functional throughout a person's lifetime.[45,47,48] The tryptophans in γ-crystallin have a low

quantum yield of fluorescence and, in time-resolved experiments show, an additional 2 ps lifetime decay that is not seen in fluorescence of tryptophan in water.[47] This quenching has been attributed to electron transfer to a backbone amide,[47,48] though additional potential quenchers, such as histidine, aspartate, and cysteine residues, are also found nearby. By transferring this energy from the UV light into transient charge-transfer states, these tryptophans may avoid other more damaging reactions.

Another protein that may have spectroscopic properties that are relevant to its function is the plant photoreceptor UVR8. This protein is normally found as a dimer, but dissociates in response to UV light in order to regulate gene transcription. The dimer interface contains 7 of the 10 tryptophan residues in each subunit. Each of these tryptophans is part of a common pentapeptide motif of Gly-Trp-Arg-His-Thr. The Arg residue of this motif projects away from the protein to form a salt bridge with carboxylate groups on the opposite subunit. Christie et al. proposed that electron transfer from Trp to Arg disrupts the necessary charge interactions to promote dissociation. They found that mutating a single tryptophan to phenylalanine alters the light-induced dissociation to respond at shorter wavelengths where phenylalanine absorbs instead of tryptophan.[39]

Explanations of Tryptophan Fluorescence Variation:

Emission Energy:

The emission wavelength of tryptophan fluorescence is commonly interpreted in terms of solvent polarity, because fluorophores that are in a more hydrophobic environment often exhibit strong blue shifts compared to tryptophans that are more exposed. While this generalization often holds true, it neglects relevant details about the emitting state. Callis and co-workers have argued

the differences in emission energy can be viewed as an "internal Stark effect".[49,50] A Stark effect refers to a shift in transition energy in response to an applied electric field. An internal Stark effect would occur when the electric field is produced by another part of the same molecule. Upon excitation of tryptophan, electron density shifts from the pyrrole end to the benzene end of the indole ring. Either a positive charge near the end with increased electron density or negative charge near the opposite end would be expected to stabilize the excited state, producing a red shift. A blue shift can be produced with the opposite arrangement of charge. This model provides reasonable predictions of the emission energy for a variety of proteins.[49,50] Callis and coworkers were also able to separate contributions to the shift that from protein and water atoms near tryptophan. Contrary to the common, but overly simplistic, view that greater solvent exposure leads to a red shift, they found both protein and water atoms could produce shifts in either direction.[50] Additional complications can affect the emission energy, however. Trp48 of azurin is strongly blue shifted, with a peak emission wavelength at 305 nm, possibly due to emission primarily from the ^1L_b state rather than the ^1L_a as is the case for most other proteins.[50,51] Proteins with short lifetimes may also appear blue shifted because the fluorescence decays before tryptophan can relax to a lower energy.[47,52,53]

Quantum Yield:

The quantum yield of a fluorophore is determined by the competition between radiative decay and non-radiative mechanisms that return the molecule back to the ground state. Much of the variation in quantum yield for tryptophan in different proteins is probably due to tryptophan acting either as a proton acceptor or electron donor.

One obvious explanation for variations in fluorescence yield would be the prescence of

possible charge donors or acceptors in the neighboring sidechains within a protein. Quenching of tryptophan fluorescence by amino acids with free carbonyl groups, imidazole, thiol or amino groups has been reported for some time.[54–57] A systematic study was undertaken by Chen and Barkley[58] using 3-methylindole (3-MI) as an analog of tryptophan. They combined 3-MI with a variety of N-acetyl amino acids in solution, allowing determination of quenching constants for the side chains. The acetylation prevented additional quenching by the free amino group. Chen and Barkly also measured deuterium isotope effects and reduction potentials to determine whether quenching occurred via proton transfer or electron transfer.

Chen and Barkley found that proton transfer could occur from tyrosine and the amino group of lysine or unacetylated glycine. A carboxylic acid or histidine could quench only when protonated; however this quenching was not isotope dependent and the quenching rate correlated with the reduction potential. This suggests that quenching occurred via electron transfer, despite the requirement for the electron acceptor to be protonated. Electron transfer involving cysteine thiol groups and cystine disulfides also was observed.

More recently, Qiu et al.[59] introduced a single tryptophan into different positions in myoglobin and observed fast quenching of tryptophan fluorescence near Gln, Glu, Cys or a cystine disulfide. Molecular dynamics simulations showed structural fluctuations bring these side chains close to the benzene ring of tryptophan. Quenching by histidine has also been used to monitor the folding in several proteins, including villin.[40–43]

While electron or proton transfer between tryptophan and the side chains of other residues can clearly quench fluorescence, such groups are not always near enough to explain all

the variations in tryptophan fluorescence. However, all proteins have multiple amides near tryptophan in the form of the peptide backbone. A difference in fluorescence between N-acetyl tryptophanamide (NATA) and 3-MI suggests that the backbone of tryptophan itself can influence protein fluorescence.[30,60] Callis and co-workers have focused on this mechanism.[42,53,61–63] They used mixed MD/QM simulations to calculate the difference in energy between the ^1L_a state and charge transfer to the peptide backbone in a variety of proteins. This energy difference could then be used to predict quantum yields for these proteins.

The calculations of Callis et al. provide a reasonable correlation with experimentally measured quantum yields,[42,61,63] suggesting that the general hypothesis is sound. However, several outliers and the need to adjust energies in order to bring calculated quantum yields in line with experiment point to an incomplete model. These discrepancies could reflect differences in the structures used in the simulations versus those used experimentally, some of which required mutations to generate proteins with a single tryptophan. Fluorescence studies often require point mutations to either remove other residues that contribute to fluorescence or to introduce a single tryptophan. As my work with COMT illustrates, these mutations themselves can alter the protein structures, so the use of native structures for calculations could be unreliable. The simulations by Callis et al. also generally were much shorter than fluorescence lifetimes[61,63] and may not have adequately sampled the conformational space responsible for the fluorescence. While some simulations took other forms of electron transfer into account,[42,61] they neglected other mechanisms such as proton transfer or resonance energy transfer. Further discrepancies could result from simplified treatment of dielectric effects, which can be complex.[64,65]

Chapter 3: Experimental Studies of Trp-Containing Peptides

Peptide Structures:

To address some of the shortcomings in the calculations by Callis and co-workers I turned to two somewhat simpler systems. These can be studied in a more systematic way to clarify specific causes of differences in fluorescence.

The hairpin system was based on the HP8 hairpin (sequence Ac-WVTIpGKKIWTG-NH_2, with lower case indicating a D-amino acid). The hairpin fold is stabilized by the edge-to-face interaction between the two tryptophan residues.[66,67] Further stabilization is provided by the WTG-NH_2 motif, which forms a cap by an interaction between Trp10 and the C-terminal amide[68] and by a π-cation interaction between Trp1 and Lys8.[66] For my studies, Trp10 was usually replaced with a Phe to provide a single fluorophore at Trp1 while varying residue 8. The structure of the His8 peptide determined by NMR is shown in figure 9A. All of the position 8 mutants adopt the same backbone structure and remain ~90% folded at room temperature as characterized by NMR and circular dichroism. We also modified the interactions between residues 1 and 10 by putting Tyr, His, Phe or Leu at residue 10 and by interchanging the Trp and Phe residues to make Phe1/Trp10, all with Ala8. These mutations were slightly destabilizing, being 64-70% folded at 12° C.

The second set of peptides used the Trp-cage16b[69] as a basis. This was a modified version of the earlier Trp-cage10b[70] with several glycine residues replaced with d-alanine (sequence DAYAQWLADaGPASaRPPPS, again with lower case indicating the D-amino acids) to give an even more stable structure (figure 9B). This peptide has a melting temperature of 83° C as

measured by circular dichroism[69] and is nearly completely folded at room temperature. For fluorescence studies the tyrosine at position 3 was replaced by a phenylalanine, and in one variant with bromo-phenylalanine, to simplify the fluorescence signal while having little effect on the stability. Additional modifications focused on the alternative ways of disrupting the putative salt bridge between Asp9 and Arg16. This site was chosen due to the hydrogen bond between the ε–nitrogen of Trp6 and the backbone carbonyl oxygen of Arg16, which seemed to be a plausible electron acceptor. Changes at residue 9 or 16 were slightly destabilizing, particularly the Arg16 mutants, though the peptides were still largely folded. The Arg16Nva and Tyr3Brf mutants used the Trp-cage 10b scaffold instead of 16b.

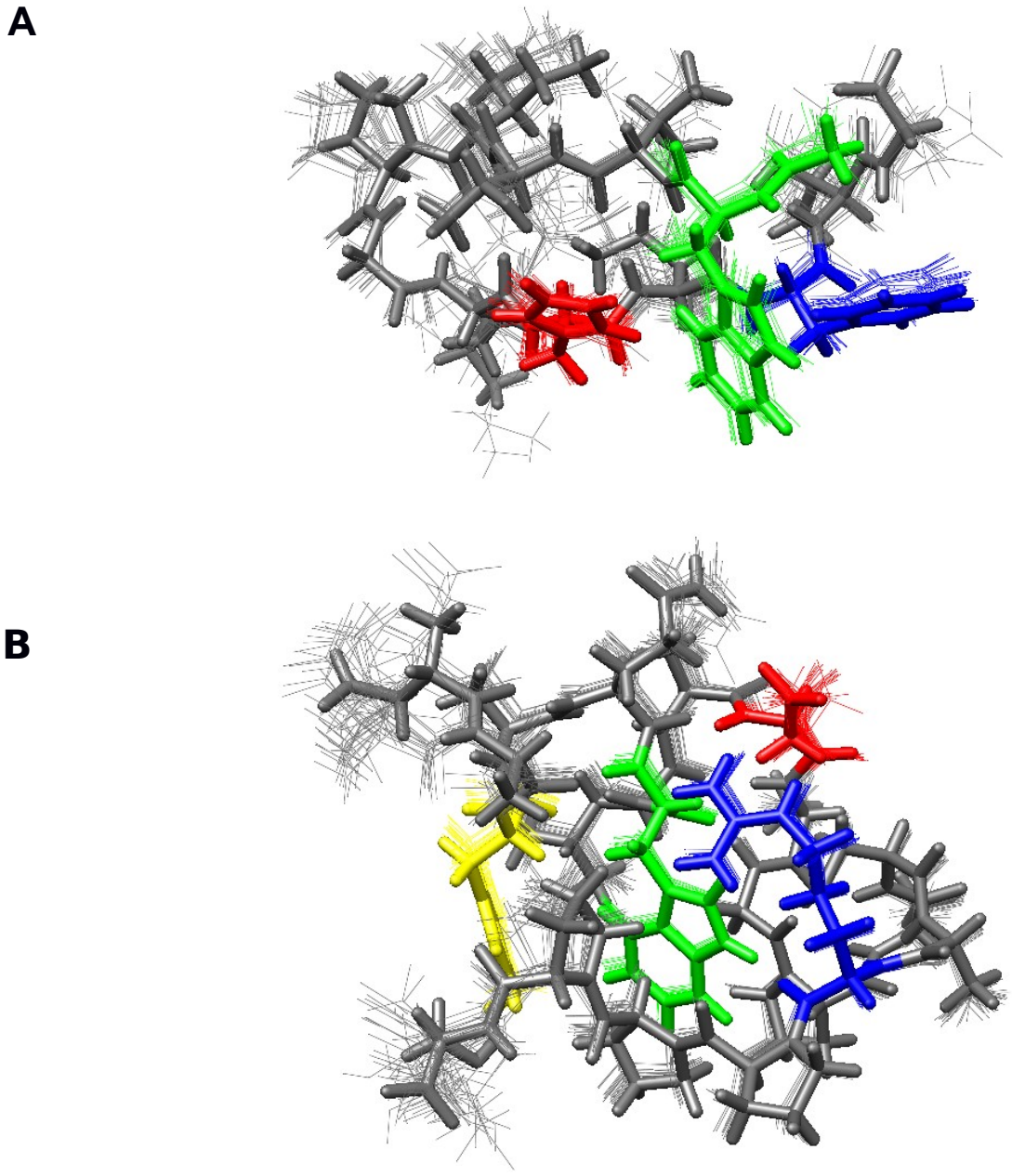

Figure 9: NMR ensembles of scaffold peptides. Structures used to start simulations or create mutant structures shown in stick representation, other parts of the ensemble shown as wire representation. (A) HP8 His8 hairpin. Trp1 colored green. Changes were made to residue 8 (red) or 10 (blue). (B) Trpcage16b. Trp6 shown in green. Changes were made to residue 9 (red) or 16 (blue). For fluorescence measurements Tyr3 (yellow) was changed to Phe or bromo-Phe.

Experimental Methods:

(This section partially reproduced from McMillan et al. 2012[71])

Peptide Synthesis:

Peptides were synthesized using 9-fluorenylmethoxycarbonyl-protected amino acids on an ABI 433A peptide synthesizer, acetylated on the resin with 4.3% triethylamine and 3% acetic anhydride in dimethylformamide, released by shaking the resin with trifluoroacetic acid with 2.5% water and 2.5% triisopropylsilane, and purified by reverse-phase HPLC. Sequences and structures were confirmed by NOESY connectivities, and purity by positive-ion mass spectrometry with a Bruker Esquire ion trap spectrometer.

Fluorescence Measurements:

Lyophilized peptide was redissolved in 10 mM potassium phosphate buffer at a final peptide concentration between 3 and 20 mM in a volume of 3 mL. Absorption spectra were measured with a Shimadzu UV-1601 spectrometer and fluorescence with a Perkin-Elmer LS-50 B fluorimeter. Emission spectra were corrected for solvent Raman scattering and the wavelength dependence of the instrument using tyrosine, tryptophan and fluorescein standards. All measurements were made at 22° C except for those on the H10, L10 and W10F1 hairpin variants, which were less stable than the other peptides at room temperature (as determined by NMR studies) and so were measured at 12° C. Some Trp-cage peptides were studied at both temperatures. Fluorescence emission spectra were typically recorded from 300 to 450 nm with excitation at 280 nm for all peptides except those containing tyrosine. For measurements of the fluorescence yield at neutral pH, the Tyr8 and Tyr10 peptides were excited at 295 nm, where absorption by tyrosine was negligible. For pH titrations of the Tyr8 and Tyr10 peptides,

excitation was done at the isosbestic point for the tyrosine residue and its anion (281 ± 5 nm for Tyr8 and 285 ± 4 nm for Tyr10) to keep the fraction of the light absorbed by tryptophan essentially constant (82.3% at 281 nm and 87.4% at 285 nm, based on the molar extinction coefficients of Trp and Tyr in water).

Emission peaks were determined by fitting the spectra to the sum of two Gaussian curves with the x-axis converted from wavelength to wavenumber and identifying the highest point. Some Trp-cage spectra had an abnormally sharp decrease in fluorescence at high energies overlapping with the Raman peak. This might have resulted from inexact subtraction of the Raman peak, which was more noticeable because of the low quantum yield of these peptides. For this reason, fitting these spectra did not use values below 307.5 nm.

Absolute quantum yields are calculated as

$$\phi_{pep} = \phi_{std} \frac{F_{pep} A_{std}}{F_{std} A_{pep}} \qquad \textit{(Equation 6)}$$

where ϕ refers to quantum yield, F is the fluorescence as defined as the area under the emission spectra and A is the absorption at the excitation wavelength and the subscripts pep and std refer to the value for the peptide or a standard. The value reported is the mean of the yields calculated using tryptophan and tyrosine as standards (ϕ_{std} = 0.13 and 0.14, respectively) and averaged over at least three samples of each peptide and three independent measurements on each sample.

Solvent isotope effects were expressed as the ratio $k_q(H_2O)/k_q(D_2O)$, where $k_q(H_2O)$ and $k_q(D_2O)$ refer to rate constants for fluorescence quenching in H_2O and D_2O, respectively. The quenching rate constant is related to the fluorescence yield by

$$k_q = k_f(\frac{1}{\phi} - \frac{1}{\phi_0}) \qquad \textit{(Equation 7)}$$

where k_f is the radiative rate constant and ϕ_0 is the fluorescence yield in the absence of the quenching process described by k_q. I assume that k_f is the same for all the peptides and is independent of the solvent. The isotope effect then is

$$\frac{k_q(H2O)}{k_q(D2O)} = \frac{1/\phi(H2O) - 1/\phi_0(H2O)}{1/\phi(D2O) - 1/\phi_0(D2O)} \qquad \text{(Equation 8)}$$

To evaluate isotope effects on the pH-dependent quenching by residues with ionizable side chains, I took ϕ_0 to be the quantum yield in the pH region where the side chains are fully deprotonated (pH > 6.0 for Asp and Glu, pH > 9.0 for His and pH > 10.0 for Orn). For Tyr and Cys, which are able to quench in both ionized and neutral form, I used $\phi_0 = 0.2475$, the mean ϕ_0 for the eight peptides with N-acetyl-Trp at position 1 and non-quenching residues at positions 8 and 10 (either Ala, Asn, Gln ε–N-acetyl-Lys, Lys, cyclohexyl-Ala, or Ser at position 8, and Phe or Leu at 10). (See below.) Absolute values of k_q were obtained by setting $k_f = 6.11 \times 10^7$ s^{-1}, which was calculated from the yield and lifetime of fluorescence from Trp in solution.[29]

Quantum Yields

Hairpins

Table 2 gives the absolute quantum yields (ϕ) of all the hairpin peptides at pH 6.5. With the exception of peptides containing Cys, His, Orn (ornithine) or Tyr at position 8 or 10, the peptides with N-acetyl-Trp at position 1 (peptides 1-10 in Table 2) have a remarkably constant ϕ of 0.251 ± 0.021, despite their varying charge and polarity. For comparison, 3-MI in water has a quantum yield of 0.34,[60] and free tryptophan and N-acetyltryptophanamide have yields of 0.13 to

0.14.[29,30] The strong quenching by Cys (ϕ = 0.04) and mild quenching by Tyr (ϕ = 0.13 at position 8 or 0.16 at position 10) compared to Ala (ϕ = 0.25) is consistent with Chen and Barkley's[58] findings on quenching of 3-MI fluorescence. In contrast, Lys at position 8 did not quench fluorescence relative to Ala. This seems likely to reflect an unfavorable position of the ε–amino group relative to the tryptophan's indole ring. Orn, which resembles Lys in having a primary amino group in its side chain but has one fewer methylene group, quenched the fluorescence by about 50% (Table 2). Interchanging the positions of Trp and Phe in the Ala8 peptide results in strong quenching (ϕ = 0.06), even though the indole ring then is far from any residue whose side chain is likely to donate or accept a proton or electron, though the several backbone amides are close.

Figure 10 shows the dependence of the fluorescence yield on pH for the hairpin peptides containing an amino acid with an ionizable side chain at position 8 or 10, along with the yield for the Ala8 peptide for comparison. The fluorescence of the Ala8 peptide was essentially independent of pH. The fluorescence of the peptides containing Asp, Glu or His, however, decreased at low pH, following titration curves consistent with protonation of the side-chain carboxylic acid (Asp and Glu) or imidazole (His) group. The fluorescence of peptides containing Orn8 or Cys8 increased at high pH where their amino or thiol side chains would be deprotonated, though the quenching relative to Ala8 remained strong in the Cys8 peptide and significant in Orn8. The fluorescence of peptides with Tyr8 or Tyr10 decreased at high pH where the phenolic side chain would be ionized. Quenching by Tyr8 was stronger than that by Tyr10 at pH 6.5, but was similar at high pH.

Although histidine, aspartate and glutamate quench only if protonated, replacing the solvent H_2O by D_2O had little or no effect on quenching (Table 3). Quenching by these residues evidently involves transfer of electrons rather than protons, in accord with Chen and Barkley's[58] results for 3-MI in solution. In contrast, replacing H_2O by D_2O decreased the rate constant for quenching by Orn8 at pH 6.5 by a factor of 8, indicating that ornithine probably quenches by proton transfer. This is similar to Chen and Barkley's observations of lysine.[58] Quenching by Tyr8 and Tyr10 showed smaller, but significant isotope effects at pH 6.5, which largely disappeared at high pH even though the quenching increased in strength (Table 2). Tyr8 and Tyr10 thus appear to quench by electron transfer at high pH, but at least partly by proton transfer at pH 6.5. Cys8 also showed a small isotope effect that diminished at high pH even though the quenching remained significant.

Trp-cages

The prototype Trp-cage peptide had a fluorescence yield of 0.01 (table 3). Replacing Arg16 by the nonionizable amino acid norvaline (Nva) or citrulline (Cit) increased the yield at 22°C by a factor of about 2, as did replacing Asp9 by Leu. These substitutions disrupt the salt bridge between Asp9 and Arg16, and thus could affect the structure or stability of the folded peptide as well as the electric fields acting on Trp6. However, neither replacing Asp9 by Ala nor the double substitution Asp9Ala/Arg16Ile, which also would disrupt the salt bridge, had a significant effect on the yield (table 3). To investigate whether the increased fluorescence of some of the variant Trp-cage peptides reflected the presence of a small amount of unfolded peptide, I also measured the yields of five of the peptides at 12°C, where the folded peptides are more stable (table 3). Lowering the temperature decreased the fluorescence yield slightly in the

Asp9/Cit16 peptide, suggesting that the higher yield relative to D9/R16 at 22°C could reflect partial unfolding. Lowering the temperature had no significant effect in the Asp9/Arg16, Ala9/Nva16 and Leu9/Arg16 variants, and even increased the yield marginally in the Leu9/Ile16 peptide. However, it is possible that effects of unfolding are masked by an intrinsic temperature dependence of the rate of a competing electron-transfer reaction. Taken together, the relatively small effects of replacing either Asp9 or Arg16 by a nonionizable amino acid indicate that the electric fields from these residues are strongly shielded before they reach the tryptophan or the electron acceptor responsible for quenching.

Emission Energy

In contrast to the variations of almost 30-fold in fluorescence yield, changes in the fluorescence emission spectra of the peptides were relatively small. The emission peaks of the β–hairpins ranged only from 340 nm (29,400 cm^{-1}) in the Cha8 peptide to 347 nm (28,800 cm^{-1}) in the Cys8 and Ala8/His10 peptides (table 2 and figure 11A). The peaks of the Trp-cage peptides ranged only from 336 to 346 nm (table 4 and figure 11B).

Table 2: Fluorescence Quantum Yields and Emission Maxima of β-Hairpin peptides at pH 6.5

Peptide [a]	Yield [b]	λ_{max} (nm) [c]
Ala8 / Phe10	0.25 ± 0.02	343
εN-acetyl-Lys8 / Phe10	0.25 ± 0.01	341
Asn8 / Phe10	0.28 ± 0.03	344
Asp8 / Phe10	0.27 ± 0.01	344
Lys8 / Phe10	0.24 ± 0.01	343
Cha8 [d] / Phe10	0.27 ± 0.01	340
Gln8 / Phe10	0.23 ± 0.02	343
Glu8 / Phe10	0.25 ± 0.03	343
Ser8 / Phe10	0.22 ± 0.01	344
Cys8 / Phe10	0.036 ± 0.001	347
Orn8 [e] / Phe10	0.113 ± 0.005	345
Tyr8 / Phe10	0.134 ± 0.003	343
His8 / Phe10	0.17 ± 0.01	344
Ala8 / Tyr10	0.166 ± 0.008	344
Ala8 / His10	0.135 ± 0.004	347
Ala8 / Leu10	0.24 ± 0.03	345
N-Ac-Phe1 / Ala8 / Trp10	0.068 ± 0.005	345

[a] Ac-**W**VTIpGK**AI****F**TG-NH_2, with the indicated substitutions for the residues in bold font (residues 1, 8 and 10). Except where indicated in the last row, all the peptides had N-acetylTrp at position 1.
[b] Fluorescence quantum yield (mean and standard deviation of 3 measurements).
[c] Emission peak ± 1 nm.

Table 3: Solvent Isotope Effects on Fluorescence Quenching in β−Hairpin Peptides

Peptide [a]	pH	$k_q(H_2O)$ (10^8 s^{-1})[b]	$k_q(D_2O)$ (10^8 s^{-1})[b]	$k_q(H_2O)/k_q(D_2O)$
Ala8 / Phe10	6.5	(0) [c]	0.18 ± 0.02	[c]
Asp 8 / Phe10	3.0	3.85 ± 0.16	2.79 ± 0.23	1.4 ± 0.1
Glu 8 / Phe10	3.0	1.63 ± 0.22	1.63 ± 0.17	1.0 ± 0.2
His 8 / Phe10	3.0	5.09 ± 0.14	4.82 ± 0.62	1.1 ± 0.1
Ala8 / His 10	3.0	9.31 ± 0.41	5.29 ± 0.40	1.8 ± 0.2
Orn8 / Phe10	6.5	2.63 ± 0.13	0.28 ± 0.03	9.3 ± 1.1
Tyr8 / Phe10	6.5	2.09 ± 0.08	1.22 ± 0.08	1.7 ± 0.2
	11.5 [d]	16.1 ± 0.71	12.7 ± 1.1	1.3 ± 0.1
Ala8 / Tyr10	6.5	1.21 ± 0.08	0.70 ± 0.19	1.7± 0.2
	11.5 [d]	30.8 ± 1.9	16.5 ± 4.6	1.9 ± 0.6
Cys 8 / Phe10	6.5	14.5 ± 0.62	8.02 ± 0.41	1.8 ± 0.2
	10.0	2.86± 0.09	2.20 ± 0.09	1.2 ± 0.1

[a] Peptides are designated as in Table 2.

[b] Rate constant for the pH-dependent quenching process in H_2O or D_2O, calculated as described in the text except for Ala8. The entries are the mean and standard deviation of 3 measurements.

[c] The fluorescence yield for Ala8 was independent of pH, and was not significantly affected by deuteration of the solvent. $\phi(H_2O)$ was 0.25 ± 0.01 and ϕ (D_2O) was 0.26 ± 0.02.

[d] The Tyr probably is not completely deprotonated at this pH.

Table 4: Trp-cage Quantum Yield and Emission Peak at pH 6.5

Peptide [a]	Yield [b]		λ_{max} (nm)[c]	
	12°C	22°C	12°C	22°C
Asp9 / Arg16	0.010 ± 0.001	0.009 ± 0.001	342	343
Asp9 / Nva16 [d,h]	0.016 ± 0.002	ND [e]	346	ND
Asp9 / Cit16 [f]	0.025 ± 0.002	0.016 ± 0.003	343	345
Ala9 / Arg16	0.010 ± 0.003	ND	336	ND
Ala9 / Nva16 [d]	0.014 ± 0.001	0.014 ± 0.00	343	343
Leu9 / Arg16	0.021 ± 0.004	0.019 ± 0.002	345	346
Leu9 / Ile16	0.008 ± 0.003	0.014 ± 0.00	346	346
Asp9/Arg16/Br-Phe3 [g,h]	0.019 ± 0.002	ND	345	ND

[a] DA**F**AQWLA**D**aGPASa**R**PPPS, with the indicated substitutions for the residues in bold font (positions 3, 9 and 16). Except for the Br-Phe peptide (last row), all the TrpCage peptides had Phe at position 3.
[b] Fluorescence quantum yield (mean and standard deviation of 3 measurements).
[c] Emission peak ± 1 nm.
[d] Nva = norvaline.
[e] ND = Not determined.
[f] Cit = citruline.
[g] Br-Phe = *p*-Br-phenylalanine
[h] These peptides were made with the Trp-cage 10b scaffold

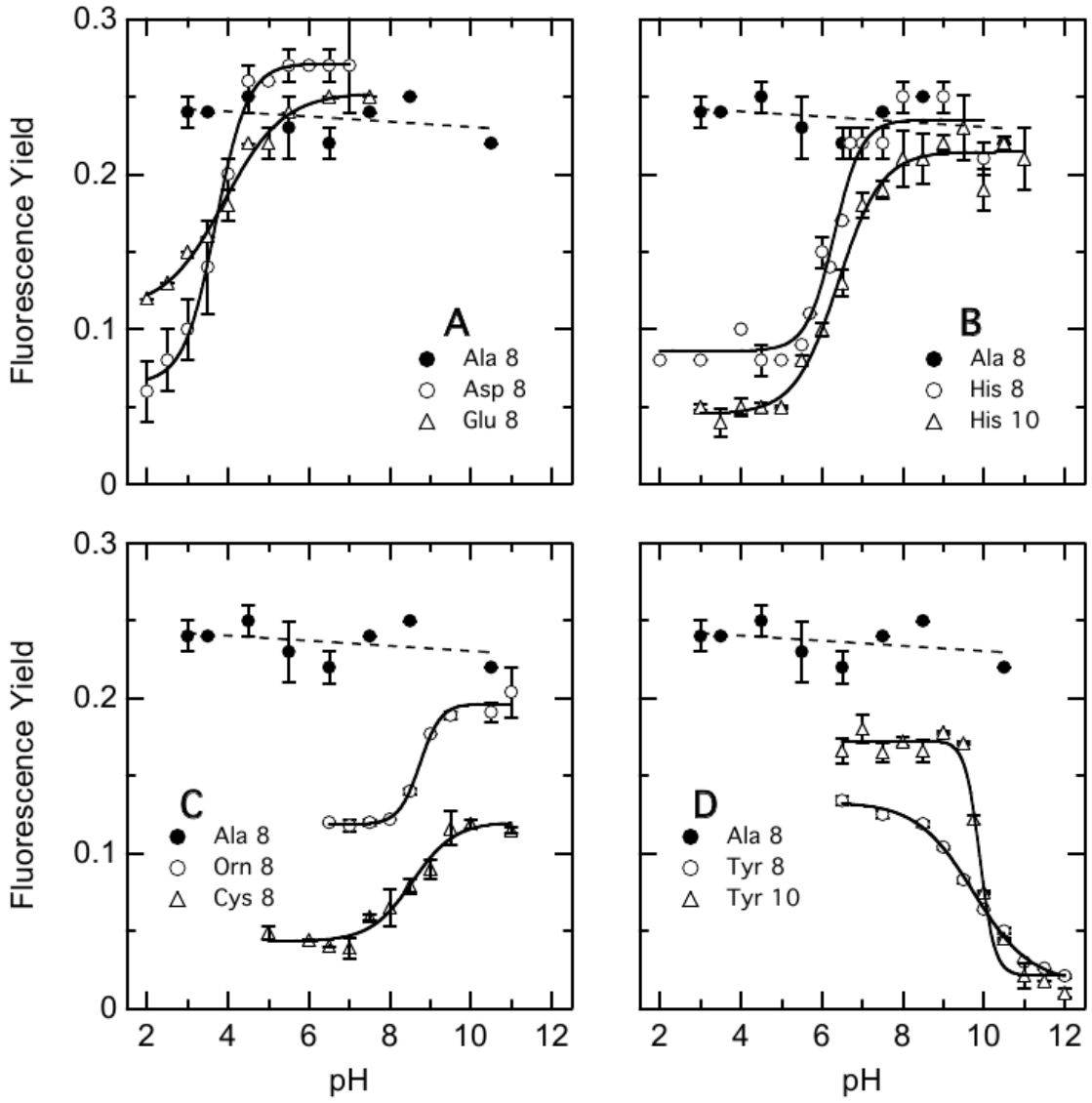

Figure 10: Fluorescence yield of hairpin peptides as function of pH. In all panels the non-ionizable Ala8 is shown as filled circles. Solid lines result from fitting data to a predicted titration curve. Open symbols show ionizable groups (A) acidic residues, (B) Histidine on either face of Trp1, (C) Other ionizable residues (not shown is Lys8 which was pH independent), (D) Tyrosine on either face of Trp1

A

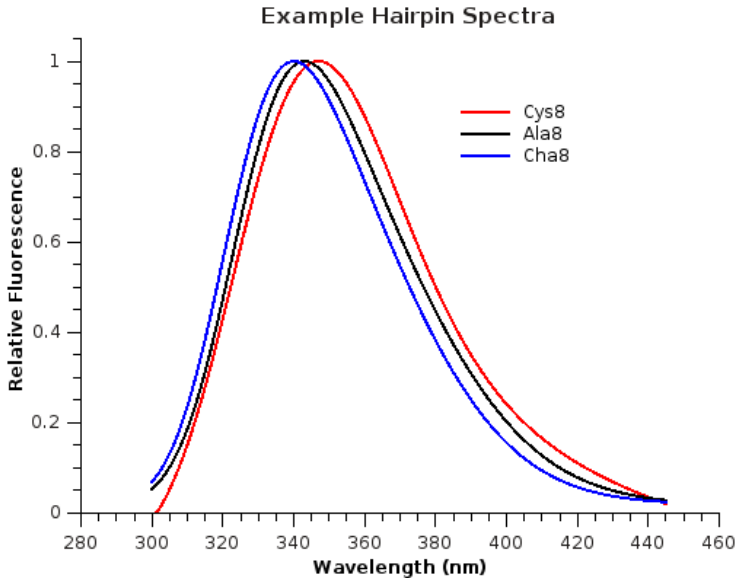

B

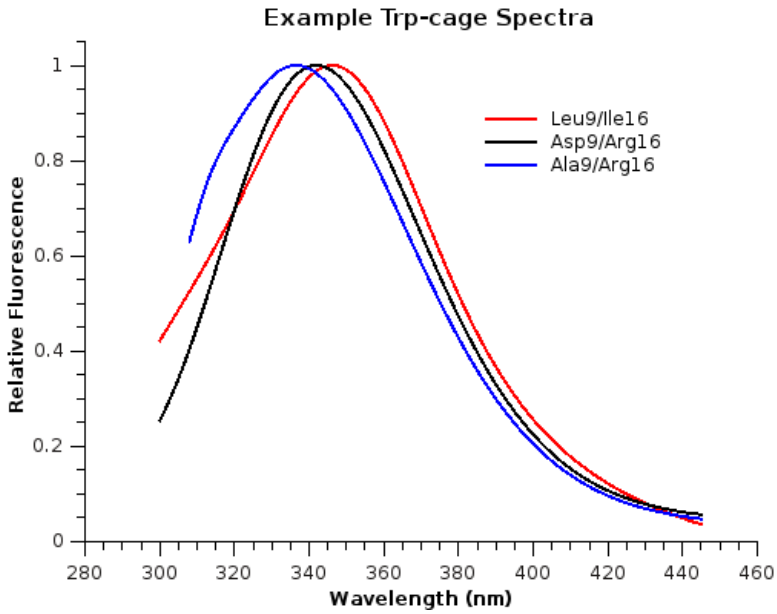

Figure 11: Fitted emission spectra of representative peptides. (A) hairpins Cha8 (blue, shortest wavelength emission) Cys8 (red, longest wavelength), Ala8 (black intermediate wavelength) (B) Trp-cages Asp9Ala (blue) shortest wavelength emission Asp9Leu/Arg16Ile (red) longest wavelength, Wildtype (black) intermediate wavelength. Spectra were fit to the sum of two Gaussian curves and are normalized to the peak.

Chapter 4: Calculation of Energies of Trp-Containing Peptides

Mixed Molecular Dynamics-Quantum Mechanics Simulations

Simulations were run using modified versions of the ENZYMIX[72] forcefield for classical dynamics and QCFF-PI[73,74] to treat a portion of charges quantum mechanically. These modifications carried out the quantum calculations to update charges at each step of the dynamics, coupling the two types of calculations more closely than is commonly used in other mixed MD-QM treatments. A schematic representation of this process is shown in figure 12, and described in detail below.

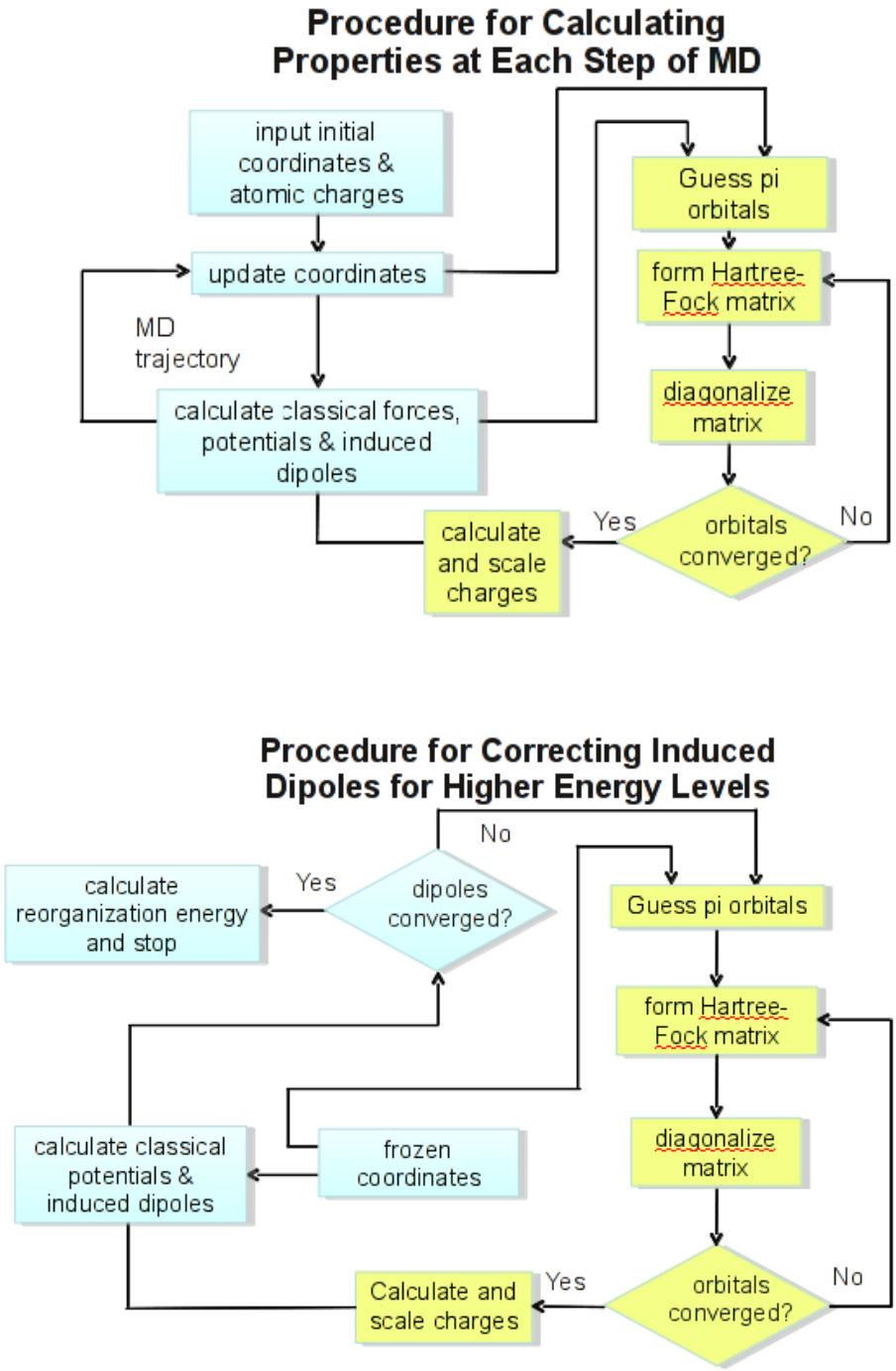

Figure 12: Schematic of Simulation Process. (A) Schematic of process of classical molecular dynamics (blue) and quantum energy calculations (yellow). (B) Schematic of optimizing induced dipoles. This was carried out on structures saved from the calculations done in (A) every 500 steps for each π–π* and charge transfer state of interest.

Classical Dynamics:

The peptide was surrounded by a flexible 3-point water molecules[75] filling a sphere with a radius of 19 Å. A quadratic pseudo-potential held the peptide at the center of the sphere and waters at the edge of the sphere, along with maintaining angular momentum at zero. Long-range electrostatic energies and forces were calculated by a multipole expansion for atoms separated by more than 12 Å for protein interactions and 20 Å for water-water interactions.[76] Parameters for the non-natural amino acids were added to the amino acid library based on existing amino acids with similar chemical groups.

Separate sets of bond length and angle parameters for the ground and excited state of indole were used as listed in Tables 5 and 6. The ground state simulations used geometry taken from a crystal structure of tryptophan.[77] The excited state simulations used geometry calculated by Callis et al. using GAUSSIAN92.[78] Bond-stretching force constants consistent with other parameters in the program were found by fitting the standard ENZYMIX force constants for C-C and C-N with various bond orders to a 2^{nd}-order polynomial in the bond length, and using the same polynomial function for the bonds in the indole ring.

Explicit hydrogen bond terms were added between atoms that form hydrogen bonds in the peptide backbone. There are four such bonds in the hairpin (two between residues 5 and 8 and two between residues 3 and 10) and eight bonds in the Trp-cage (in each turn of the helix of residues 2 through 9 and between residues 6 and 11, 10 and 13, 11 and 14 and 12 and 15). These bonds were assigned ideal H–O distances of 1.95 Å and N–H–O angles of 180^{o}, bond-stretching force constants of 20 kcal mol^{-1} $Å^{-2}$ and bending force constants of 5 kcal mol^{-1}. The results were

not very sensitive to changes in these parameters. The ε–amino group of Lys7, which is located relatively far from the other groups of interest and is well solvated and presumably accompanied by a counterion, was given a net charge of zero, though using a charge of +1 had little effect on the results.

Table 5: Bond Stretching Parameters

Bond		**Ground State**		**^1L_a**	
atom *i*	**atom *j***	b_0^a	f_b^b	b_0^a	f_b^b
CG	CD1	2.344	474.7	1.428	375.9
CG	CD2	1.451	356.6	1.400	403.8
CD1	NE1	1.377	430.5	1.354	455.1
NE1	CE2	1.391	413.9	1.416	391.2
CE2	CZ2	1.400	403.8	1.377	430.5
CE2	CD2	1.382	424.4	1.414	389.2
CZ2	CH2	1.399	404.9	1.502	325.9
CH2	CZ3	1.386	419.7	1.364	447.1
CZ3	CE3	1.397	407.1	1.423	380.5
CE2	CD2	1.412	391.2	1.462	348.6
NE1	HE	0.980	434.0	0.980	434.0
CZ2	HZ1	1.000	340.0	1.000	340.0
CE3	HE2	1.000	340.0	1.00	340.0

[a] Equilibrium bond length in units of Å
[b] Bond streching force constant in units of kcal/mole

Table 6: Bond Angle Parameters

Angle			Ground -State	^1L_a
atom i	**atom j**	**atom k**	θ_0	θ_0
CB	CG	CD1	128.0	130.0
CB	CG	CD2	126.5	127.3
CD1	CG	CD2	105.5	102.6
CG	CD1	NE1	111.5	111.0
CD1	NE1	CE2	107.4	111.8
NE1	CE2	CZ2	129.0	132.7
NE1	CE2	CD2	107.8	104.7
CZ2	CE2	CD2	123.2	123.3
CG	CD2	CE3	131.2	131.3
CG	CD2	CE2	107.7	111.6
CE2	CD2	CE3	121.1	117.2
CZ3	CE3	CD2	114.6	122.8
CH2	CZ3	CD2	124.8	120.5
CZ2	CH2	CE3	119.7	119.6
CE2	CZ2	CZ3	116.4	118.8

[a] Equilibrium bond angle in units of degrees
[b] Angle bending force constant in units of kcal/mole

Quantum Calculations:

The energies and charges of the fluorophore and plausible charge transfer acceptors and donors were treated with a modified version of QCFF-PI.[73,74] This semi-empirical Hartree-Fock treatment sums the electric potentials from all non-quantum atoms at the π orbitals and includes these values in the diagonals of the Fock matrix. QCFF-PI uses this matrix to solve equations to produce a self-consistent field, diagonalizes the configuration-interaction (CI) matrix for a given number of configurations, and calculates new charges for the atoms being treated quantum mechanically. These charges are used for calculating the forces and induced dipoles of the next step of MD. Quantum charges include both a "core" charge from the nuclei and the σ electrons, which are calculated following the Del Re method[79] and held constant through out the simulation, and π charges that vary in response to fluctuating electric fields. QCFF-PI also calculates excitation energies and oscillator strengths for π–π* and charge transfer states. While more accurate energies may be calculated using a larger basis set or considering doubly-excited configurations, the simpler treatment used by QCFF-PI allows calculations to be done quickly enough that longer MD trajectories with tight coupling between classical and quantum subsystems are possible.

The original QCFF-PI treatment does not consider resonance integrals between atoms that are connected by 2 or more bonds or have orthogonal p-type wavefunctions. This fails to account electron transfer between different groups of π orbitals, such as electron transfer from tryptophan to a backbone amide or another sidechain. To add these contributions into the calculation we followed the treatment from Alden et al.[80]

Under this treatment, the ground state wavefunction of each group is assigned such that

$$\sum_{n \in a} C_{n,i}^2 \approx 1 \qquad \text{(Equation 9)}$$

where $C_{n,i}$ is the coefficient for the p_z orbital of atom n in the wavefunction ψ_i for each of the π atoms in group *a.* Configuration-interaction matrix elements for a singlet π–π* excitation localized to a single group *a* ($\psi_{a1} \rightarrow \psi_{a2}$) coupled with charge transfer to or from group *b* ($\psi_{a1} \rightarrow \psi_{b2}$ or $\psi_{b1} \rightarrow \psi_{a2}$) are then written as

$$H_{a1 \rightarrow a2, a1 \rightarrow b2} = \sum_n C_{n,a2} \sum_m C_{m,b2} \beta_{n,m} \qquad \text{(Equation 10)}$$

and

$$H_{a1 \rightarrow a2, b1 \rightarrow a2} = \sum_n C_{n,a1} \sum_m C_{m,b1} \beta_{n,m} \qquad \text{(Equation 11)}$$

$\beta_{n,m}$ is the resonance integral for the p_z electrons of atoms *n* and *m,* which can be split into two canonical π and σ componants by defining direction cosines $\eta_{x,n}$, $\eta_{y,n}$, and $\eta_{z,n}$ for atom *n* and $\eta_{x,m}$, $\eta_{y,m}$, and $\eta_{z,m}$ for atom *m*

$$\beta_{n,m} \approx \eta_{y,n}\eta_{y,m}\beta_\sigma + (\eta_{x,n}\eta x, m + (\eta_{z,n}\eta_{z,m})\beta_\pi \qquad \text{(Equation 12)}$$

The semi-empirical resonance intregrals were found to be

$$\beta_\sigma = -2.73 \times 10^6 exp(-1.95 r_{t1,t2}) - 1.81 \times 10^4 exp(-0.7 r_{t1,t2}) \qquad \textit{(Equation 13)}$$

$$\beta_\pi = 2.80 \times 10^5 exp(-1.95 r_{t1,t2}) + 3.89 \times 10^2 exp(-0.7 r_{t1,t2}) \qquad \textit{(Equation 14)}$$

where $r_{n,m}$ is the interatomic distance in Å and energies are in eV. This treatment observes the directional dependence of atomic π overlap integrals, but uses a generic distance dependence based on rates of long-range electron transfer in proteins.[81]

Excited states were identified as a local π–π* state of a particular Trp, Tyr, His, Asp, or Glu residue, or in some cases as a mixed (exciton) π–π* state, by calculating the oscillator strength attributable to atoms of each residue. Charge-transfer transitions were assigned by identifying groups of atoms for which the summed changes in charge were > 0.5 for electron donors. In some cases the transfer of electrons appeared to be distributed between two acceptors. In these cases charge acceptors were classified as the acceptor with the largest increase in electron density, though these states were rare (appearing in the first 16 states ~10% of the time or less). Transitions with dominant CT character also were recognizable by large changes in permanent dipole moment (typically > 15 D), zero or very small oscillator strengths, and the sensitivity of their energies to fields from the surroundings.

Induced Dipoles:

The polarization of atoms can have significant effects on energies of excited states.[82] To account for these effects we treated the induced dipoles, μ, on a atom, *i*, as a linear function of the electric field:

$$\vec{\mu}_i = \alpha_i \vec{E}_i = \alpha_i(\vec{E}_i^{crg} + \vec{E}_i^{ind}) \qquad \textit{(Equation 15)}$$

where α_i is the polarizability of the atom and E_i^{crg} and E_i^{ind} are the electric field at atom i from permanent and induced dipoles respectively. To prevent catastrophic polarization of atoms that approach each other closely, we followed the treatment described by Thole[83] in which the atomic charges are viewed as being distributed around the atom, rather than as at single point. This treatment uses a scaled distance ν_{ij}

$$\nu_{ij} = a r_{ij}(\alpha_i \alpha_j)^{1/6} \qquad \textit{(Equation 16)}$$

where r_{ij} is the inter-atomic distance and a is a dimensionless parameter that is independent of the type of atom. Swart and Van Duijin[84] showed that if the charge density decreases exponentially with distance, the electric potential at i will decrease by the factor f_n

$$f_{\nu,ij} = 1 - (\frac{1}{2}\nu_{ij} + 1)exp(-\nu_{ij}) \qquad \textit{(Equation 17)}$$

relative to the potential from a point charge. The field will similarly be attenuated by

$$f_{E,ij} = f_{\nu,ij} - \frac{1}{2}(\nu_{ij}^2 + \nu_{ij})\exp(-\nu_{ij}) \qquad \textit{(Equation 18)}$$

and the gradient of the field by

$$f_{T,ij} = f_{E,ij} - \frac{1}{6}\nu_{ij}^3\exp(-\nu_{ij}) \qquad \textit{(Equation 19)}$$

With these attenuation factors the fields E_i^{crg} and E_i^{ind} are given by

$$\vec{E}_i^{crg} = \sum_j f_{E,ik}Q_j\frac{\vec{r}_{ij}}{r_{ij}^3} \qquad \text{(Equation 20)}$$

$$\vec{E}_i^{ind} = \sum_{j\neq i} f_{T,ij}(\vec{\mu}_j\vec{r}_{ij})\vec{r}_{ij}/r_{ij}^5 - f_{E,ij}\vec{\mu}_j/r_{ij}^3 \qquad \text{(Equation 21)}$$

where Q_j is the charge of atom j and $\vec{r}_{ij}$ is the vector from atom j to atom i. In our treatment, the sums over j omit atoms connected to atom i by 1, 2 or 3 bonds. Bernardo et al.,[85] Burnam and Xantheas,[86] Ren and Ponder[87] and Elking et al.[88] have used similar treatments based on other possible distributions of charge density.

Swart and Van Duijin[84] found a and α for H, C, N, O and S atoms by fitting the calculated polarizabilities to the measured polarizability of 52 different molecules. We used the same value

for *a* but scaled their polarizability by 0.5 to provide consistency with ENZYMIX. This was done by optimizing calculated and measured water dipoles as will be described.

Calculating induced dipoles can be computationally expensive due to the need to recalculate the wavefunction and charges on quantum atoms in response to the changing induced dipoles. Furthermore, each excited state of interest has to be calculated independently as the induced dipoles relax around the different charge distribution. However the change in charge between each MD step is small enough that the induced dipoles of an atom can be approximated by

$$\vec{\mu}_{i,n} = \alpha(\vec{E}^{crg}_{i,n} + (\vec{E}^{ind}_{i,n-1}) \qquad \textit{(Equation 22)}$$

where n and n-1 refer to the step of the simulation and the preceding step. This simplification was used for the course of dynamics in either the ground or excited state. Every 500 ps of simulation time structures were saved and used to optimize induced dipoles for π–π* and electron transfer states that were of interest.

The calculation of excitation energies using these induced dipoles does not account for the energy that is needed to produce the dipoles themselves. This energy was calculated classically and added to the quantum mechanical excitation energy. The total excitation energy can then be approximated as

$$\Delta E^{0}_{k,n} = \frac{1}{2}(\Delta E^{g}_{k,n} + \Delta E^{e}_{k,n}) \qquad \textit{(Equation 23)}$$

where $\Delta E^{g}_{k,n}$ is the transition energy with induced dipoles optimized for the ground state and $\Delta E^{e}_{k,n}$ is the transition energy with induced dipoles for the excited state (both including the

classical energy of creating the induced dipoles). Values for oscillator strength and dipole moments were calculated in a similar manner.

Estimated Amount of Quenching:

An estimate of the quenching by electron transfer is given by

$$Q_f = \sum_i \langle \frac{1}{2} \frac{V_i(t)^2}{Z(t)} (1 - \frac{\delta_i(t)}{\sqrt{\delta_i(t)^2 + 4V_i(t)^2}}) \rangle \qquad \textit{(Equation 24)}$$

$$Z(t) = \sum_i [\frac{V_i(t)^2}{2} (1 - \frac{\delta_i(t)}{\sqrt{\delta_i(t)^2 + 4V_i(t)^2}})] + \zeta \qquad \textit{(Equation 25)}$$

where $V_i(t)$ is the electronic coupling between a charge transfer state *i* and the first π–π* at time *t*, $\delta_i(t)$ is the difference in energy for these states, and ζ is a parameter related to the rate of electronic dephasing caused by fluctuations of the energy gaps or decay of the excited state by processes other than electron transfer. This gives a fraction of the expected fluorescence that would be quenched by electron transfer. It can be converted to a quantum yield by multiplying by the value of φ_0 that was used in equation 7. Substituting Q_f into equation 7 would give an expected rate of quenching,

$$k_q = k_f (\frac{1}{Q_f \phi_0} - \frac{1}{\phi_0}) \qquad \text{(Equation 26)}$$

Neglecting correlation between $\delta_i(t)$ and $V_i(t)$ equation 24 goes to zero when $\delta_i(t) >> |V_i^2(t)|$ or $|Z(t)| >> |V(t)^2|$. The latter of these conditions describes a nonadiabatic electron transfer reaction.

Under the nonadiabatic limit a proper treatment of quenching should approximate the classical Marcus equation[89] which was used by Callis and co-workers[61]

$$k_{et} = (\frac{4\pi^2}{h})V^2(4\pi\lambda k_B T)^{-1/2} exp(-\frac{(\Delta G_0 + \lambda)^2}{4\lambda k_B T}) \qquad \text{(Equation 27)}$$

where λ is the reorganization energy. The average of our $\delta_i(t)$ over a trajectory ($<\delta_i(t)>$) should be equivalent to the activation free energy ($(\Delta G_0+\lambda)^2/4\lambda k_B T$) that appears in the exponential of Equation 27. However the function described by Marcus theory decreases as $\Delta G_0+\lambda$ increases, in either the positive or negative directions. Equation 24 differs, by assuming electron transfer can still occur even when $\delta_i(t) << 0$ (figure 13A). This is likely to be the case because a quasi-continuum of excited vibrational levels of a charge-transfer state can come into resonance with the π–π^* states even if the difference in zero-point levels is negative.[90–92]

Equation 24 also applies under the adiabatic limit where $|Vi(t)|$ is large. Although Callis and co-workers calculated coupling factors ~20 to 90 times the value of 10 cm^{-1} they initially assumed,[63] they continued to use that value and equation 27 for later studies where the adiabatic limit could apply.[42,53] The major approximations of the treatment I use come from not considering nuclear relaxation following electron transfer and not considering possible interference between parallel electron transfer reactions.

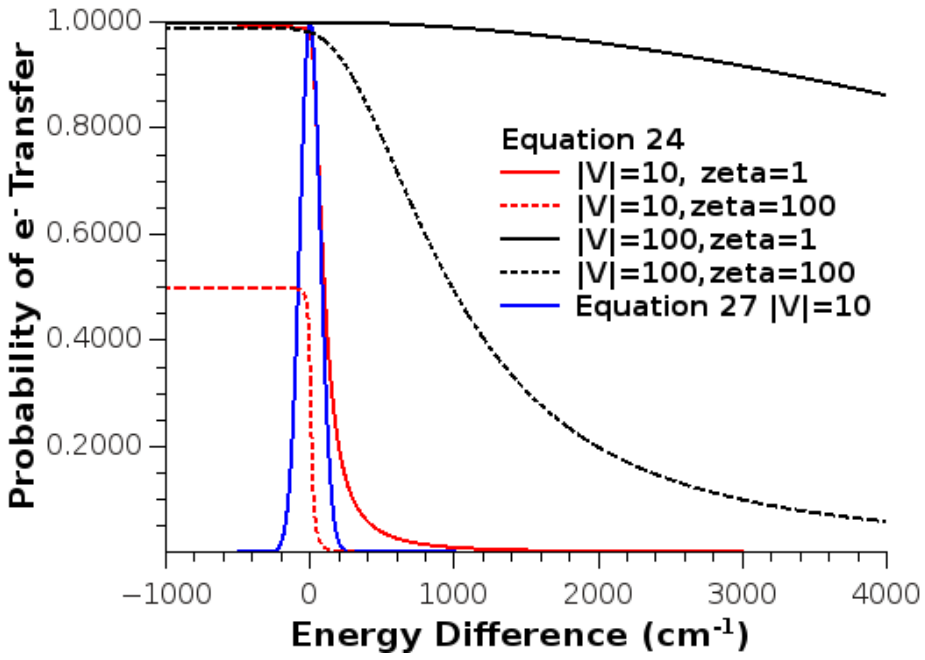

Figure 13: Different treatments effect of energy differences on predicted quenching. Red and black compares equation 24 in a nonadiabatic and adiabatic regimes, respectively. Blue shows the expected rate under Marcus theory[89] The Marcus theory rate is normalized at the peak to the probability of 1 for the other treatments. Solid lines show $\zeta = 1$ and dotted lines set to 100.

Simulation Conditions:

Simulations for parameterizing water used a sphere with a radius of 21 Å which included 1419 water molecules. One water molecule was used to define the center of the system, while the others were free to diffuse. The system was equilibrated by Monte Carlo rotations with simulated annealing from 325 to 25 K, followed by MD trajectories of 10 ps at 30 K and 20 ps at 300 K. Multiple MD trajectories then were propagated for 500 ps in 1-fs steps at 300 K, and the structural coordinates and atomic charges were saved every 0.5 ps for analysis. The scaling factor for atomic polarizabilities (see above) and the van der Waals parameters for water hydrogens (A_H and B_H, where the energy of van der Waals interactions between atoms *i* and *j* is written $A_iA_jr_{ij}^{12}$ -$B_iB_jr_{ij}^{-6}$) were varied to optimize the agreement of the calculated and measured properties. Other parameters were standard for the ENZYMIX force field (atomic charges -0.80 and 0.40 for water O and H atoms, respectively, and van der Waals parameters A_O = 793.0 $kcal^{1/2}mol^{-1/2}Å^6$ and B_O = 25.0 $kcal^{1/2}mol^{-1/2}Å^3$ for water oxygens).

The starting structure for peptide simulations was the first listed in the structure determined by NMR for the HP8 His8/Phe10 hairpin and the wildtype Trp-cage. Tyr3 of the Trp-cage was changed to Phe. Starting structures for other peptides were generated using a Monte Carlo procedure that optimized the side-chain torsion angles of the new residue while holding the backbone fixed.[93] The protein was surrounded by a water sphere with a radius of 19Å which included ~1066 water molecules. The energy of these waters was minimized using Monte Carlo rotation similar to that of the all water simulations, followed by a 10 ps MD trajectory at 30 K. After this relaxation, simulations were run in the ground state for at least 2.4 ns at 300 K with structures saved every ps for analysis. Twenty 500 ps trajectories in the excited state were started

from these saved structures, beginning at 500ps and following 100 ps intervals. Structures were saved from these excited state trajectories every 0.5ps for optimizing induced dipoles and calculating energies.

Calculated Results

Water parameterization:

Because the tryptophan and possible charge donors and acceptors are all exposed to solvent, it is important that the simulations reprodcuce the electrostatic properties of water. Spheres of water were simulated with different scaling of the atomic polarizabilities (α from the equation 15 in the induced dipole discussion) and van der Waals parameters (A_H and B_H where the van der Waals energy between atoms i and j is written in the form of $A_iA_jr_{ij}^{-12} + B_iB_jr_{ij}^{-6}$). The best reproduction of experimental values used $A_H = 0.10$ kcal$^{1/2}$mol$^{-1/2}$Å^6, $B_H = 0.20$ kcal$^{1/2}$mol$^{-1/2}$Å^3, and scaled the polarizabilities determined by Swart and Van Duijin by 0.50. The mean dipole moment of water was calculated to be 2.95 debye, with a permanent dipole of 2.34 D and the distribution of dipoles shown in figure 14. This is in agreement with the measured dipole moment of 2.95± 0.2 D[85] and *ab initio* MD calculations done by Silvestrelli and Parrinello,[94] who found the same mean, though a broader distribution. This could be due to a smaller water sphere (12 Å vs 21Å for our simulations), which would have been more subject to edge effects. Similar dipoles were also found by others.[85–87]

Radial distribution functions for O-H and O-O distances (g_{OH} and g_{OO}) match closely with values determined by neutron scattering. Figure 15a shows the distribution for g_{OH} with a peak at

2.73 Å, while 14b shows the distribution for g_{OH} with peaks at 1.74 and 3.23 Å, which are within 0.05 Å of measured peaks.[95,96]

The geometry of individual waters also matches well with the reports of others as shown in Table 7. The mean bond length was 1.015 Å, in agreement with the experimental value of 1.01 Å reported by Soper and Benmore,[95] but somewhat greater than the 0.97 Å measured by Ichikawa et al.[97] and Silvestrelli and Parrinello's[94] *ab initio*-MD value of 0.991 Å. The mean bond angle of 106.0° matches both the measured angle[97] and the value obtained by *ab initio* MD calculations.[94]

Table 7: Water Geometry

Source	H-O-H Bond Angle	O-H bond length (Å)
Calculated by ENZYQ	106.0	1.015
Calculated by Silvestrelli and Parrinello[94]	106.0	0.991
Ichikawa et al.[97]	106.0	0.97
Soper and Benmore [95]	N/A	1.01

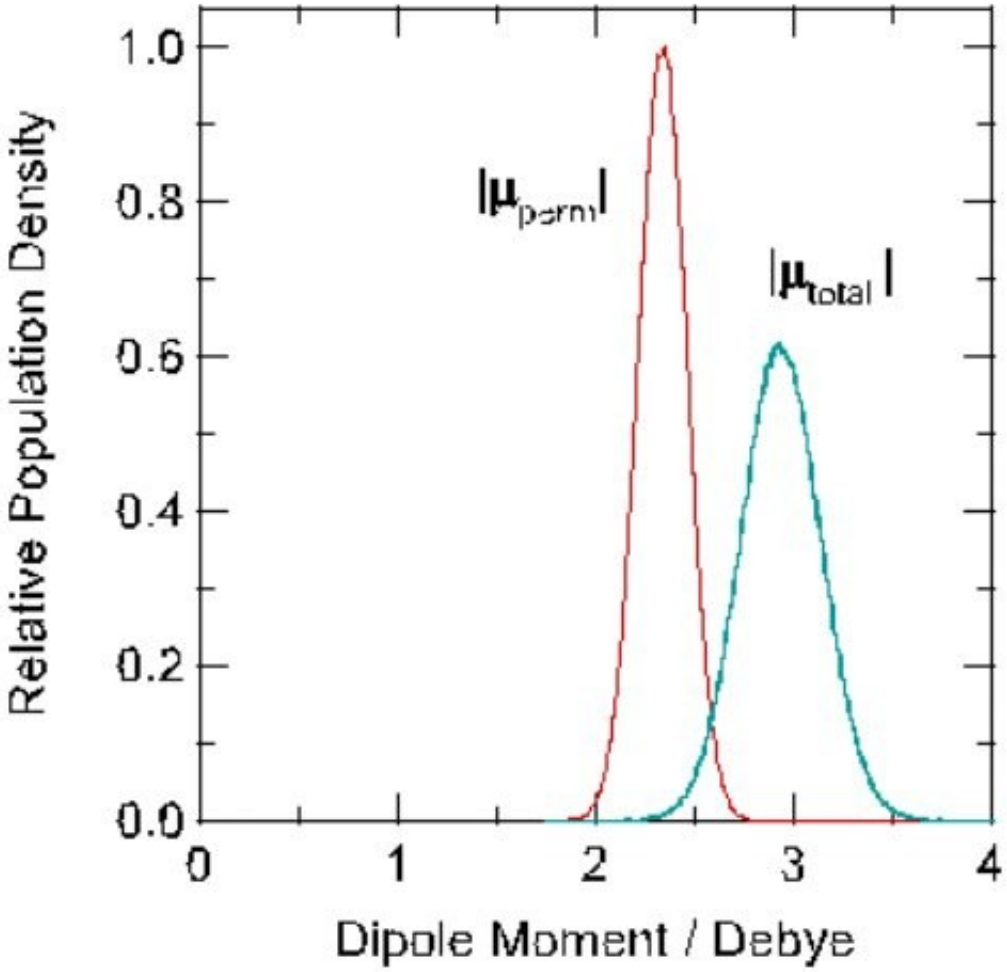

Figure 14: Distribution of calculated water dipoles red shows dipole of permanent charges, blue shows total dipole including induced dipoles.

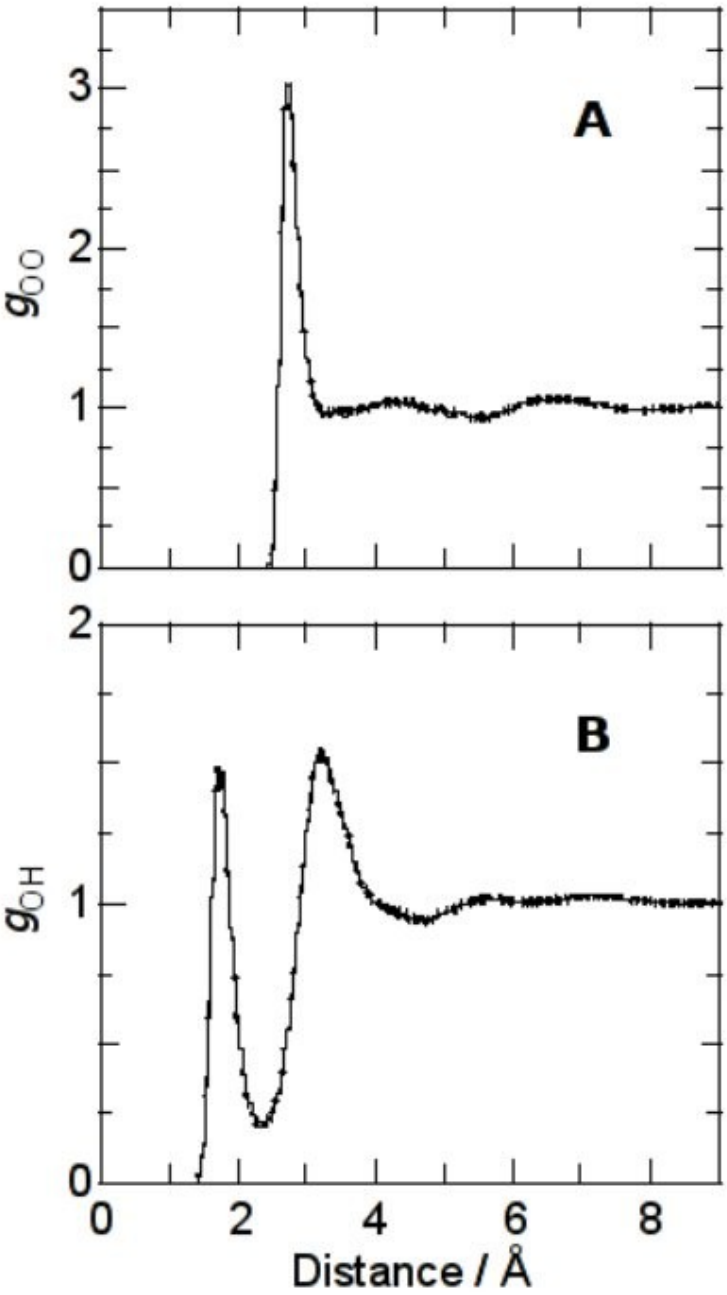

Figure 15: Radial Distribution functions for water (A) Radial distribution of oxygen-oxygen distances. (B) Radial distribution of oxygen-hydrogen distances.

Charge Scaling Parameterization:

Callis et al. found it was necessary to scale charges that were calculated using INDO/S-CIS before using them in molecular dynamics calculations.[50,61] Using the unscaled quantum charges gave too strong of an interaction between protein and water atoms, and scaling down by 20% resulted in better agreement with experiment. This was determined by fitting calculated emission energies to the experimental values.

Fitting our calculated energies to experimental emission energies in a similar way is problematic due to the small variation of emission energy in the peptides being studied. To test how similar scaling affected ENZYQ with an independent system, 3-MI, simulations were run *in vacuo* and in water to try to optimize calculated solvent shifts. Both the total electric fields at the quantum atoms and the charges that were calculated were varied individually over a range of scaling factors from 0.6 to 1.1. The experimentally observed[50,98] solvent shift could be reproduced by scaling charges by 1.05 as shown in figure 16. However, calculations using these scaling factors still overestimated the emission and absorption energies. The emission energy was particularly sensitive to the scaling factor being used, while absorption seemed relatively independent.

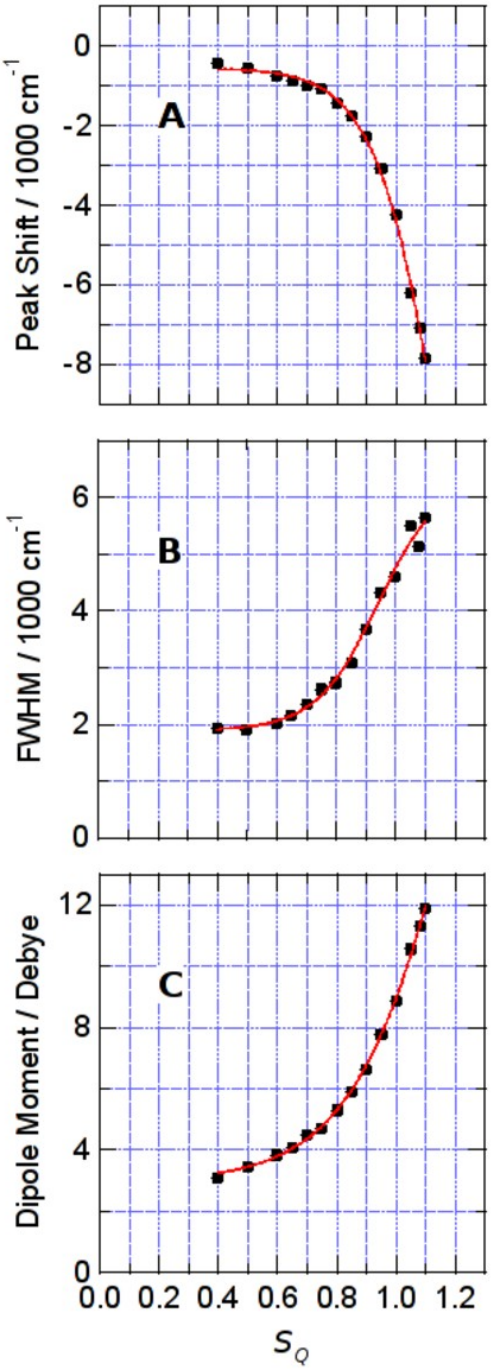

Figure 16: Calculated properties of 3-MI as a function of scaling quantum charges A shows the solvent shift of the emission energy in water relative to a vacuum. B shows the width of the distribution of energies. C shows the average permanent dipole of the excited 3-MI molecule.

Since it was not possible to use a single scaling factor that reproduced all of the properties of 3-MI, I turned to adjusting the scaling factor with the full peptides. Scaling fields or charges had similar effects in peptide simulations. The peptides' overall structure could be maintained regardless of scale factor, though scaling charges down led to a slight decrease in the C-α root mean square deviation (RMSD) from the starting structures. The higher scaling factors which worked better for 3-MI cause more fluctuations in charge-transfer energies and also increased the probability that the self-consistent field of the quantum calculations would fail to converge.

In addition to decreasing fluctuations in charge-transfer energy, scaling affected the average charge-transfer energy for some electron acceptors. However the direction of this effect depended on the peptide scaffold, with scaling down tending to decrease the charge transfer energy in the hairpins, while increasing it in the Trp-cage system. This may be due to the different level of solvent exposure in the two systems. The minimum average charge-transfer energy of the Trp10/Phe1 hairpin was found somewhere between a scale factor of 0.6 and 0.8. Ultimately we chose to use a scale factor of 0.8 for the charges and keep the fields unscaled. This choice gives the greatest overlap in energy between the π–π* states and charge transfer states in peptides that quench by an isotope independent mechanism while minimizing large fluctuations in energy. The exception was the Lys8 hairpin, which still had frequent low energy states.

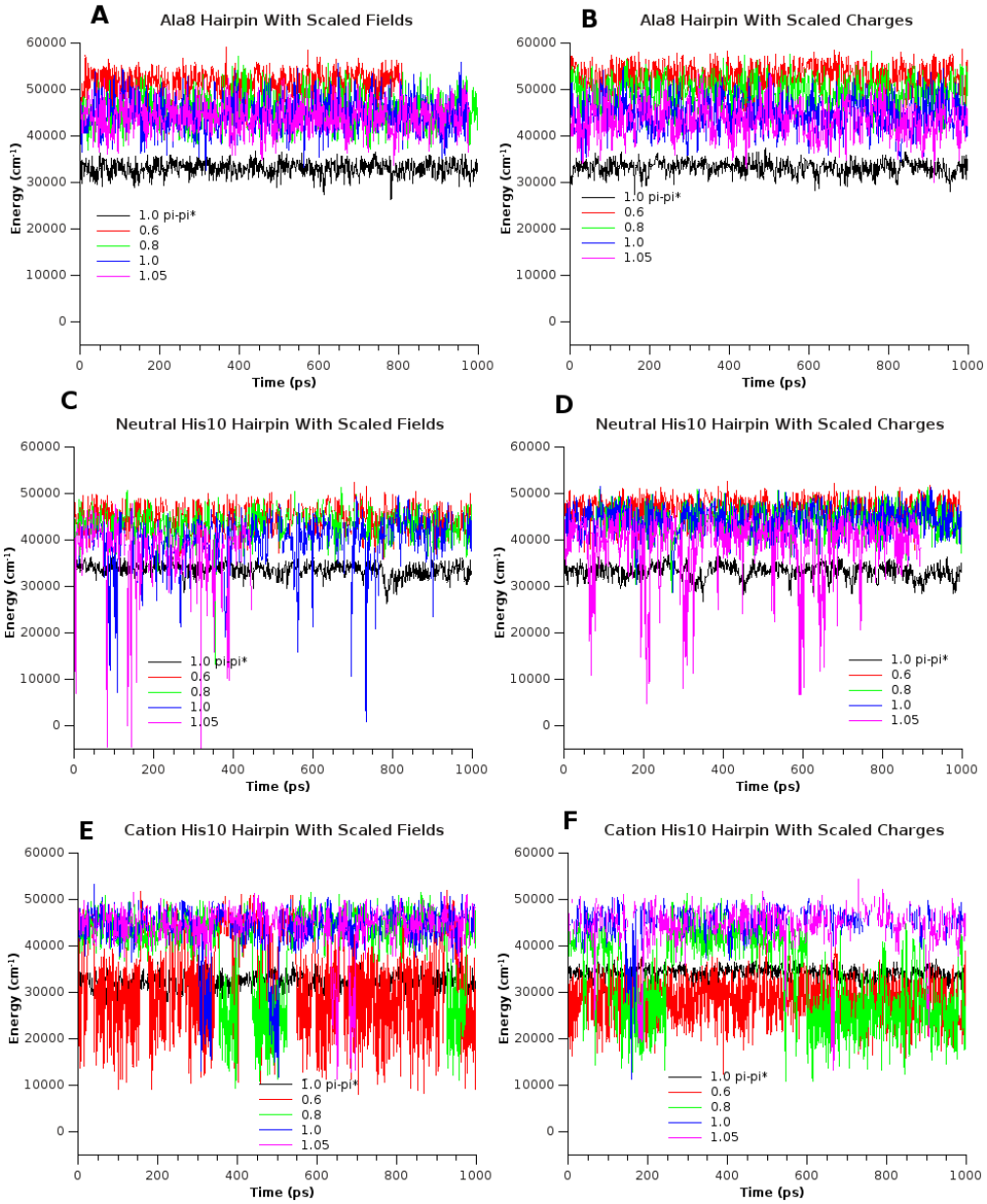

Figure 17: Examples of the influence of the charge scaling factor on charge transfer energies. Left panels used scaling of electric fields; right, scaling of calculated charges. All panels show the lowest π–π* state (black) and the lowest charge transfer state with scaling of 0.6 (red), scaling by 0.8 (green), no scaling (blue), and scaling by 1.05 (magenta)

Charge Transfer Energy Calculations:

(This section partially is reproduced from McMillan et al. 2012)[71]

All the peptides except the Arg16Cit Trp-cage mutant remained well folded during simulated trajectories in the ground or first excited singlet state, with the root-mean-square deviation (RMSD) of the C-α atoms from their initial positions generally staying below 1.5 Å and the fluctuations about the mean positions of the C-α atoms (RMSF) occurring mainly at the N- and C-termini. Figures 18 and 19 show plots of the C-α RMSD and RMSF from typical trajectories of peptides in the ground state.

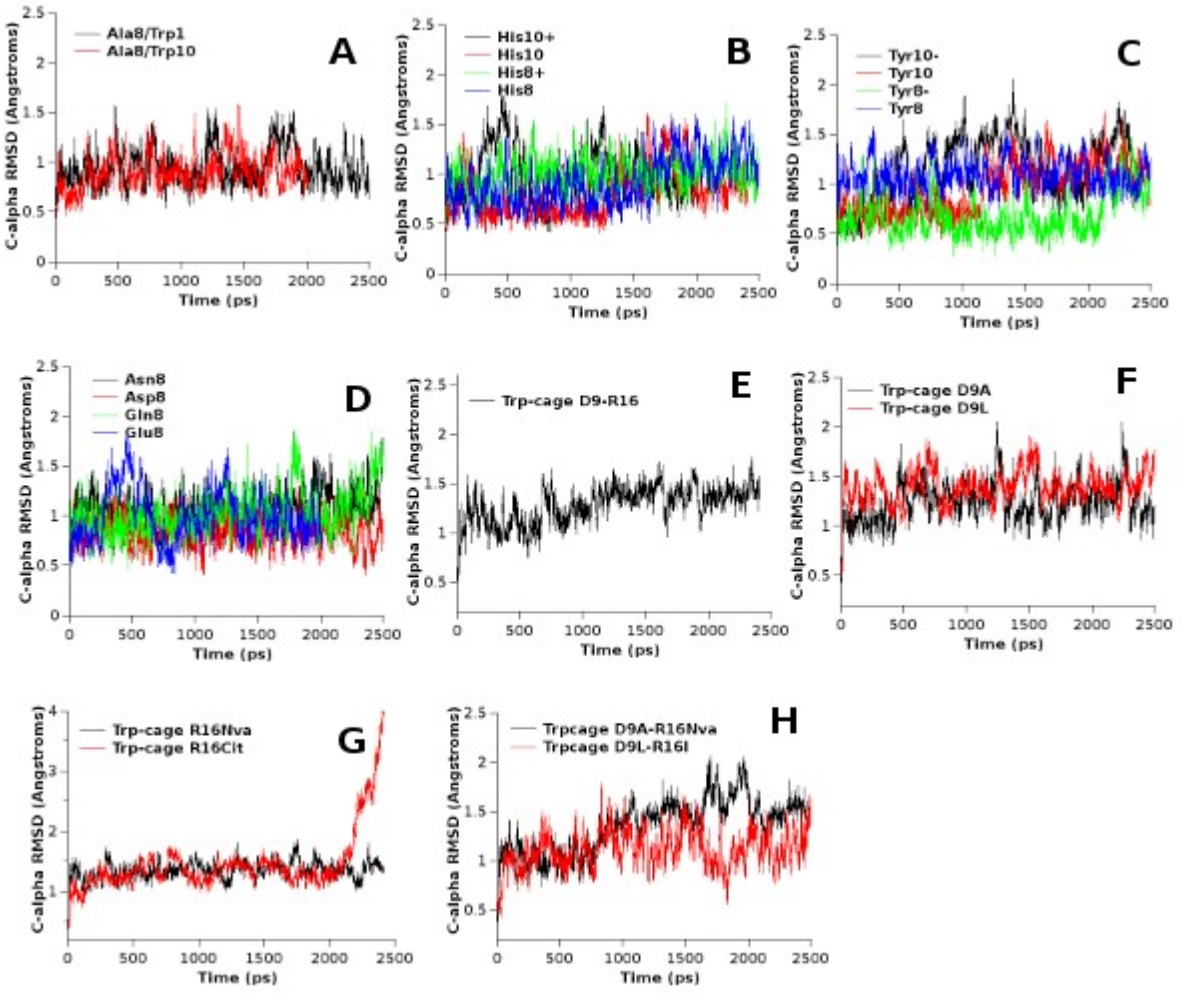

Figure 18: Representative C-α root mean square deviation from starting structure over the course of ground-state trajectories.

A

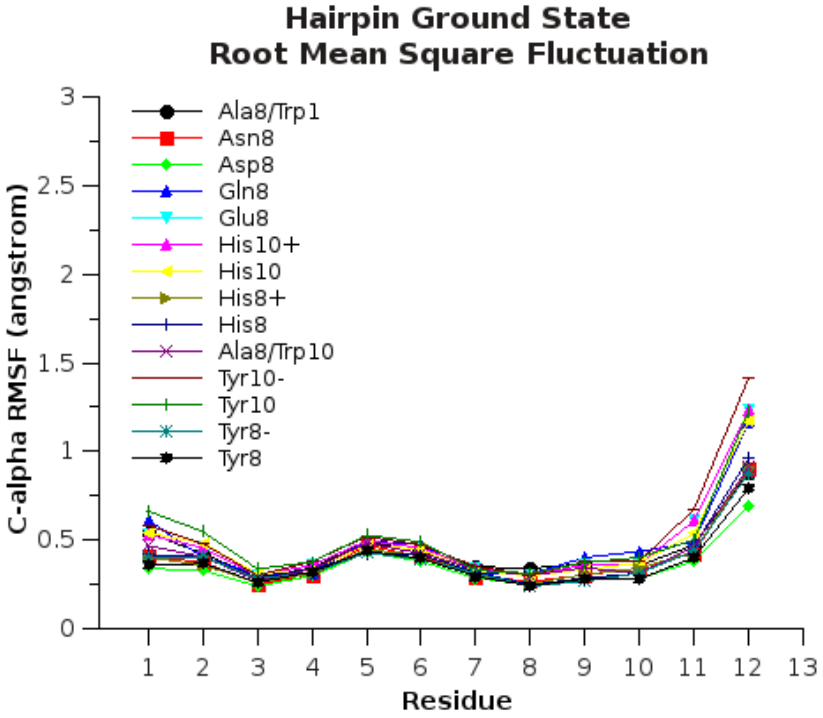

B

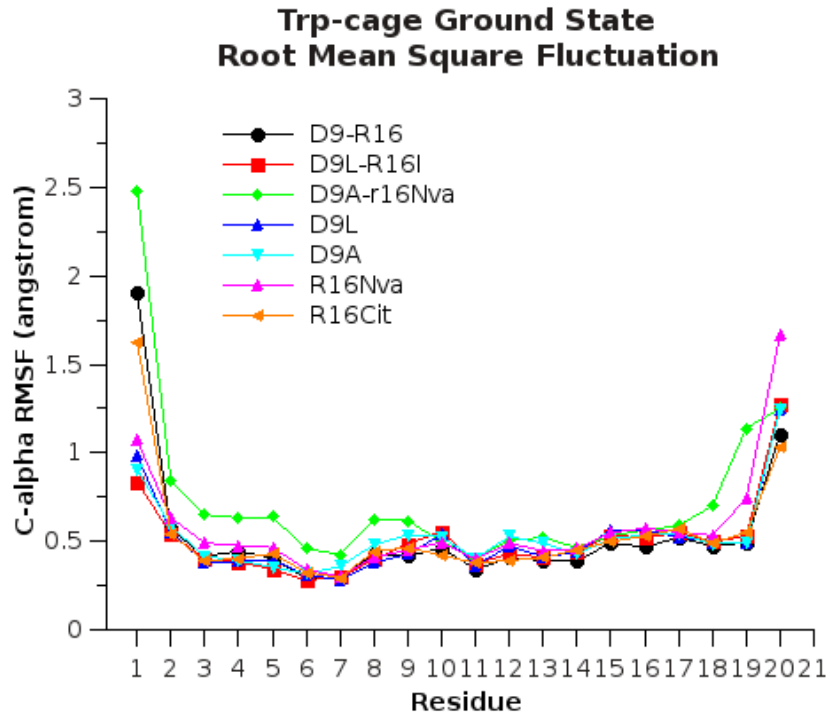

Figure 19: Representative plots of C-α root mean square fluctuations over the course of the ground state trajectories. Hairpins from the same trajectories shown in figure 18 are in A, Trp-cage peptides in B.

Figure 20A shows the energy distribution for the Ala8 hairpin peptide with tryptophan at position 1. Except for rare excursions to lower energies, the CT states of the Ala8 peptide all lie well above the π–π* states. Similar high energies (not shown) were calculated for the CT states of hairpin peptides with Cha, Ser, and ε–N-acetyl-Lys and Orn at position 8, which also did not quench by electron transfer. Interchanging the positions of Trp (originally at position 1) and Phe (originally at position 10) in the hairpin peptide moves the indole ring closer to the backbone amides formed by the amino and carboxyl groups of the Trp, as well as to the amide connecting Thr11 and Gly12, and to the N-terminal amide cap of Phe1. Three of these amides evidently are well positioned to act as electron acceptors, forming CT states with calculated energies often below the energy of the first excited π–π* state (see the curves labeled Trp -> a1, Trp -> a11 and Trp ->a12 in Figure 20B). The thermodynamically favorable electron transfer to these amides appears to provide a reasonable explanation for the decreased fluorescence of this peptide (Table 2). Electron transfer from the indole ring to the amide on the amino side of Trp10 (Trp -> a10 in Figure 20B) is less favorable, but still overlaps the π–π* states to a significant extent.

Figure 21 shows the coupling element ($|V_i(t)|$)for the major charge transfer states of the Ala8 hairpins with Trp at either position 1 or 10. Electron transfer from Trp1 to backbone amides was unfavorable due to weaker coupling in addition to having high energies. In the Trp10 peptide, Trp to a12 has the lowest energy; however figure 21B shows this state to have weaker coupling than the Trp to a11, though still somewhat stronger than in the coupling in the Trp1 hairpin. The very strong Trp to a11 coupling could favor this CT state despite its slightly higher energy.

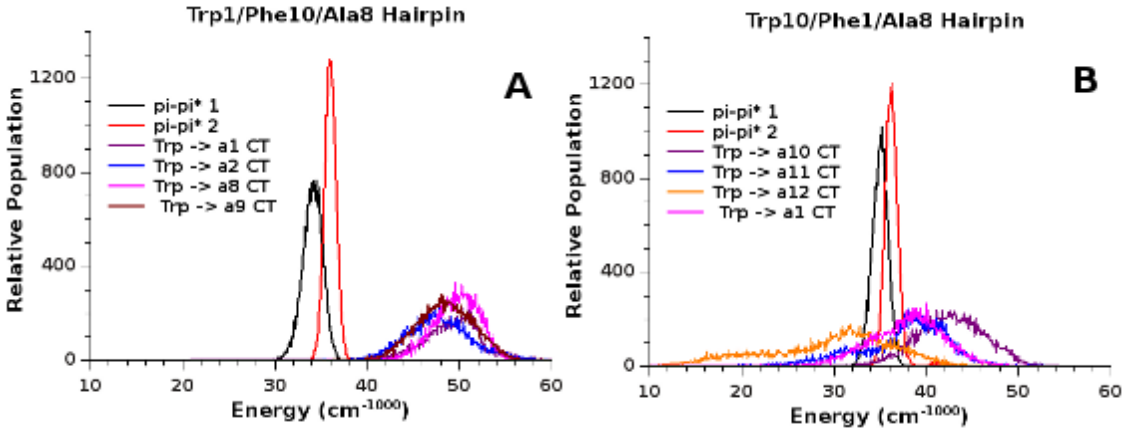

Figure 20: Ala8 Hairpin Energy Distributions Distribution of π–π* and 4 lowest energy charge-transfer energies of combined 20 simulations of Ala8 peptides with Trp at position 1 (A) or 10 (B). Notation Trp -> aX refers to charge transfer from Trp to the backbone amide of amino acid number X.

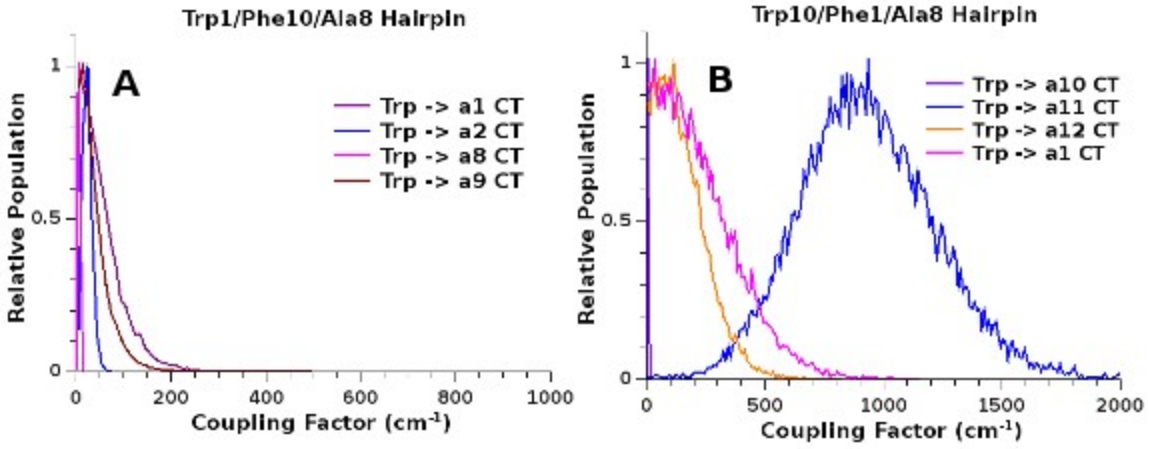

Figure 21: Ala8 Hairpin Coupling Matrix Elements. Curves are colored the as figure 20. Values are normalized to 1 at the highest point.

Other non-quenched peptides generally had low coupling constants similat to that shown in figure 21A. Because these states also have a much higher energy than the π–π* transitions, they would be be very unlikely to transfer an electron. However they still commonly had higher coupling factors than 10 cm-1 use by Callis and co-workers in their calculations.[61]

Calculations for the hairpin peptides with Trp at position 1 and neutral histidine at either position 8 or position 10 show the CT states well above the π–π* states, as in the Ala8 peptide (figure 22*A*, *B*). When the His side chain is protonated, the energy of charge transfer from the indole ring to the imidazole generally falls below the energies of the π–π* states (figure 22*C*, *D*). Charge transfer from the indole to two backbone amide groups also moves lower in energy in the protonated His8 peptide (curves Trp -> a8 and Trp -> a9 in figure 22*C*). The strong quenching of fluorescence at low pH in these peptides (Table 2 and figure 11*A*) thus could be explained by electron transfer from the indole to either the protonated imidazole side chain or to the peptide backbone.

Figure 23 shows the coupling for the His8 and His10 peptides. In both peptides the neutral (A and B) and charged (C and D) histidines had CT states with a broad distribution of strong coupling factors. His8 and His10 differ in which state had strong coupling. Electron transfer to the His sidechain was strongly coupled in the His8 peptide. In the His10 peptide, electron transfer to the His sidechain was weakly coupled, and electron transfer to a backbone amide was more strongly coupled.

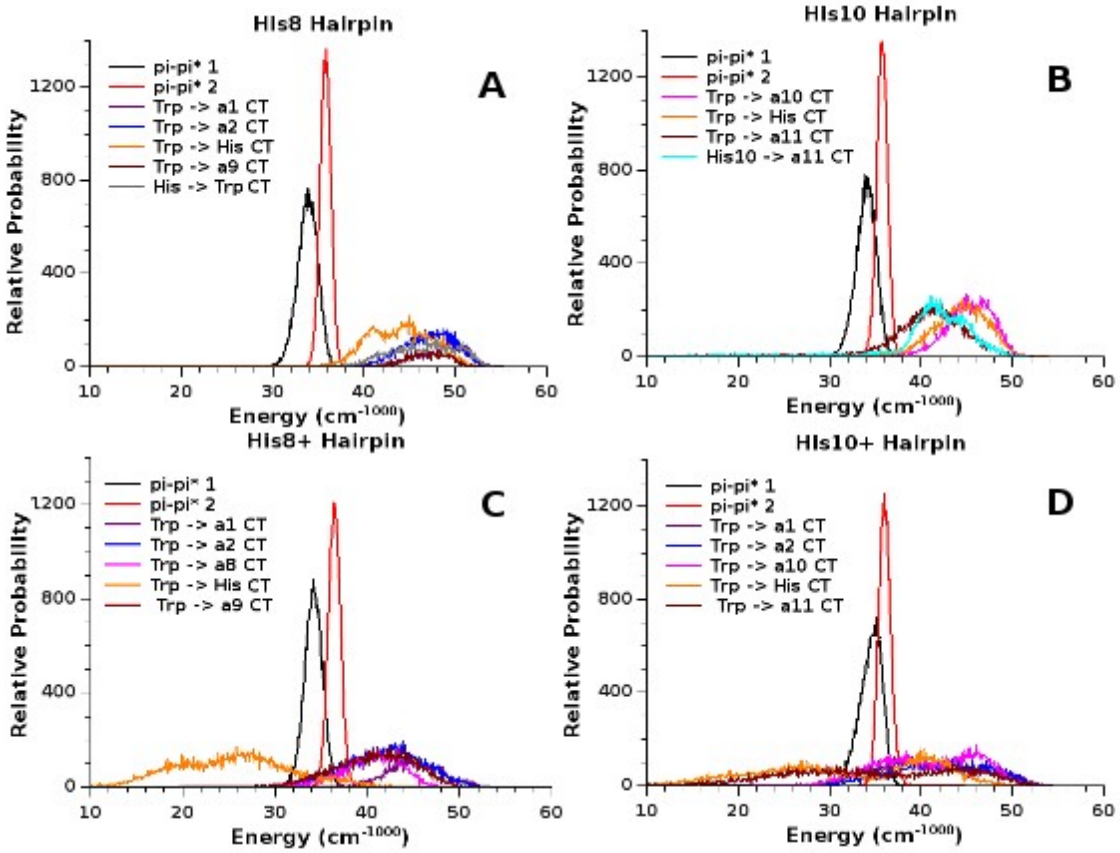

Figure 22: His Hairpin Energy Distributions Distribution of π–π* and charge transfer energies of combined 20 simulations of His8 (A and C) and His10 (B and D). The top panels show simulations of neutral histidine, bottom, protonated histidine. Charge transfer involving amides designated as in figure 20; charge transfer involving side chains uses amino acid abbreviation

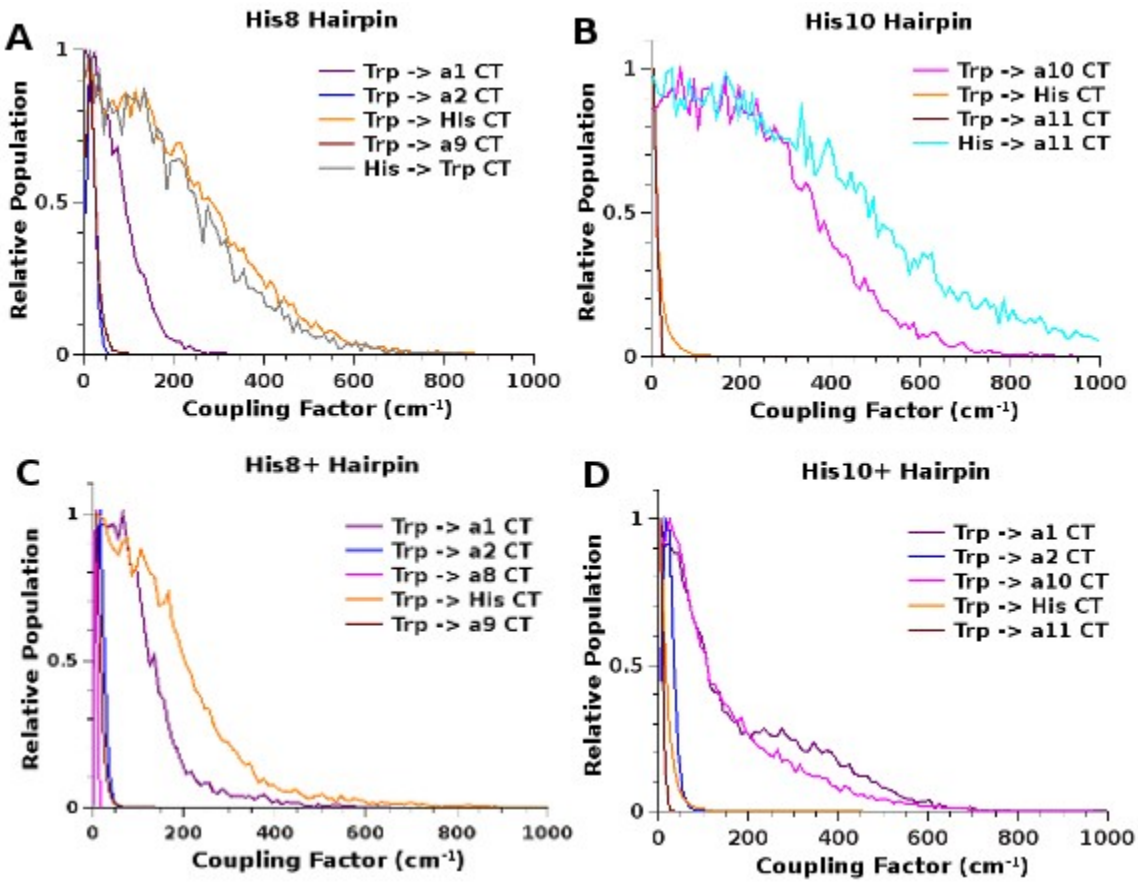

Figure 23: His Hairpin Coupling Matrix Elements: Curves for various states are colored as in figure 22, and normalized as in figure 21

Figure 24 shows the distributions of calculated energies for hairpin peptides with Trp at position 1 and either Asn, Gln, protonated Asp or protonated Glu at position 8. In the peptides containing Asn or Gln, the CT states lie largely above the first two π–π* states, while electron transfer from the indole of Trp1 to the carboxylic acid side chain is favorable in the peptides containing Asp or Glu. Replacing Asn by Asp or Gln by Glu also makes charge transfer from the indole to a backbone amide favorable. The low-lying CT states are consistent with the strong quenching of fluorescence seen in the Asp and Glu peptides at low pH (figure 11*A*), but not in the corresponding peptides containing Asn or Gln.

Asp8 and Asn8 both had stong coupling for all charge transfer to the sidechain (figure 29A and C), which also had the lowest energy for Asp8 (figure 22). In both peptides the peak of the distribution of coupling elements was at ~100 cm^{-1}, though Asp8 had a longer tail extending as high 1000 cm^{-1}. Gln8 and Glu8 also had similar levels of coupling strengths (figure 29B and D), but unlike the Asx peptides had only small coupling to the Trp to sidechain electron transfer.

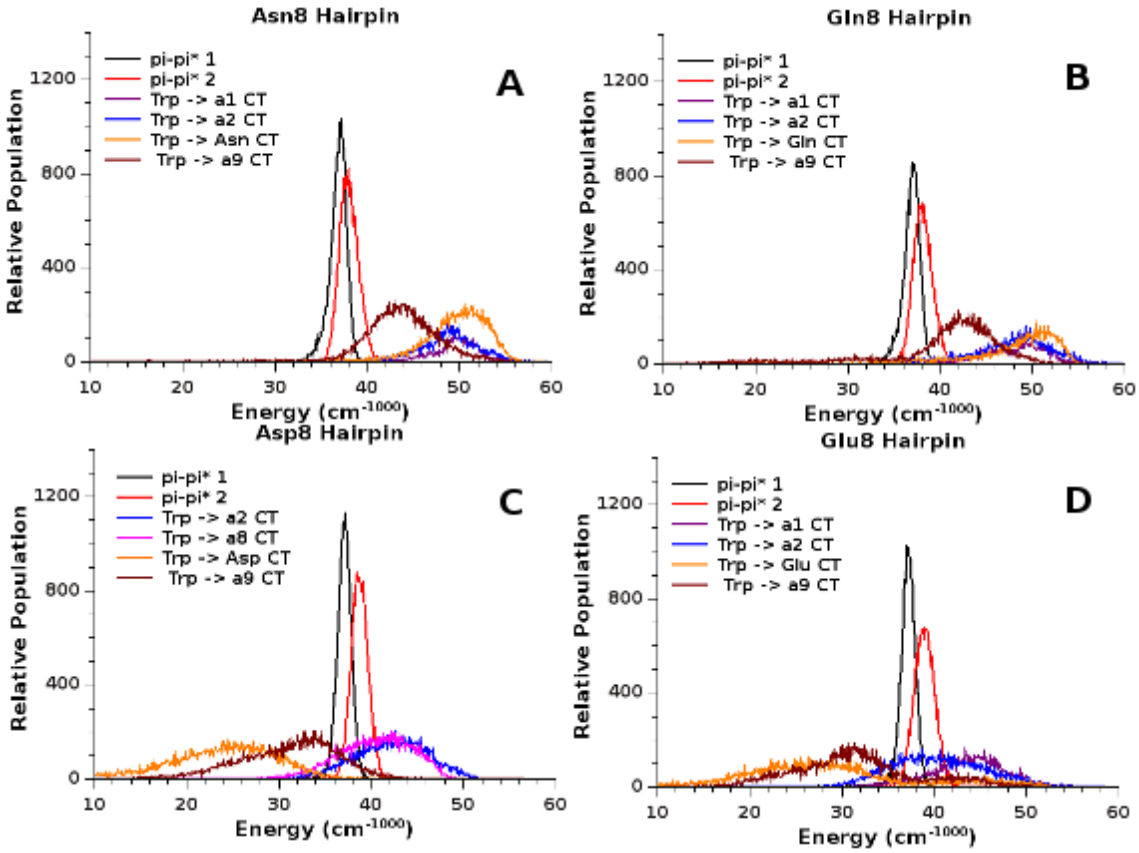

Figure 24: Carbonyl Sidechain Hairpin Energy Distributions Distribution of π–π* and 4 lowest energy charge transfer energies of combined 20 simulations of Asn8 (A), Gln8 (B) and protonated Asp8 (C) and Glu8 (D). Charge transfer involving amides designated as in figure 20, charge transfer involving side chains uses amino acid abbreviation

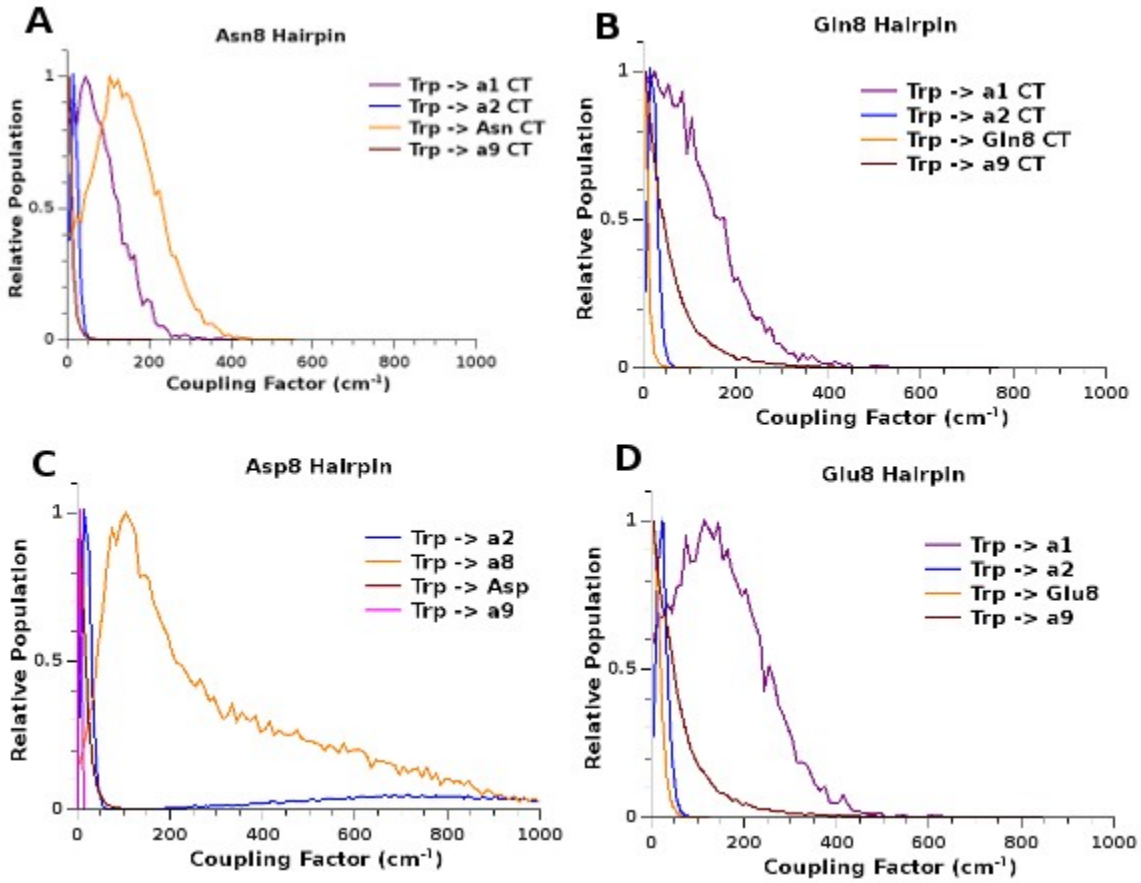

Figure 25: Carbonyl Sidechain Hairpin Coupling Matrix Elements: Curves for various states are colored as in figure 24, and normalized as in figure 21

The hairpin peptides with Tyr at position 8 or 10 had low charge transfer energies when the phenolic side chain was ionized (figure 26), in accord with the quenching of fluorescence at high pH (figure 11D). In these systems, the tyrosine's phenolate side chain serves as the electron donor, with either the indole ring of the Trp or a backbone amide group acting as the acceptor. In addition, the phenolate ring has a low-lying π-π* state that mixes with the excited states of the Trp by exciton interactions (figure 26C and D). Charge-transfer states in which an electron moves from the Tyr to a backbone amide (e.g., Tyr -> a11 in figure 26D) could form either from this state, or by electron transfer from the Tyr to the excited Trp followed by transfer from Trp to the amide.

The neutral Tyr8 and Tyr10 hairpins had a few states with high coupling factors, ranging up to 400 cm^{-1}. (figure 27A and B) The tyrosine anions also have several states with broad distributions of coupling factors, with the coupling for the lowest energy state being as high as 1000 cm^{-1}. (figure 27C and D)

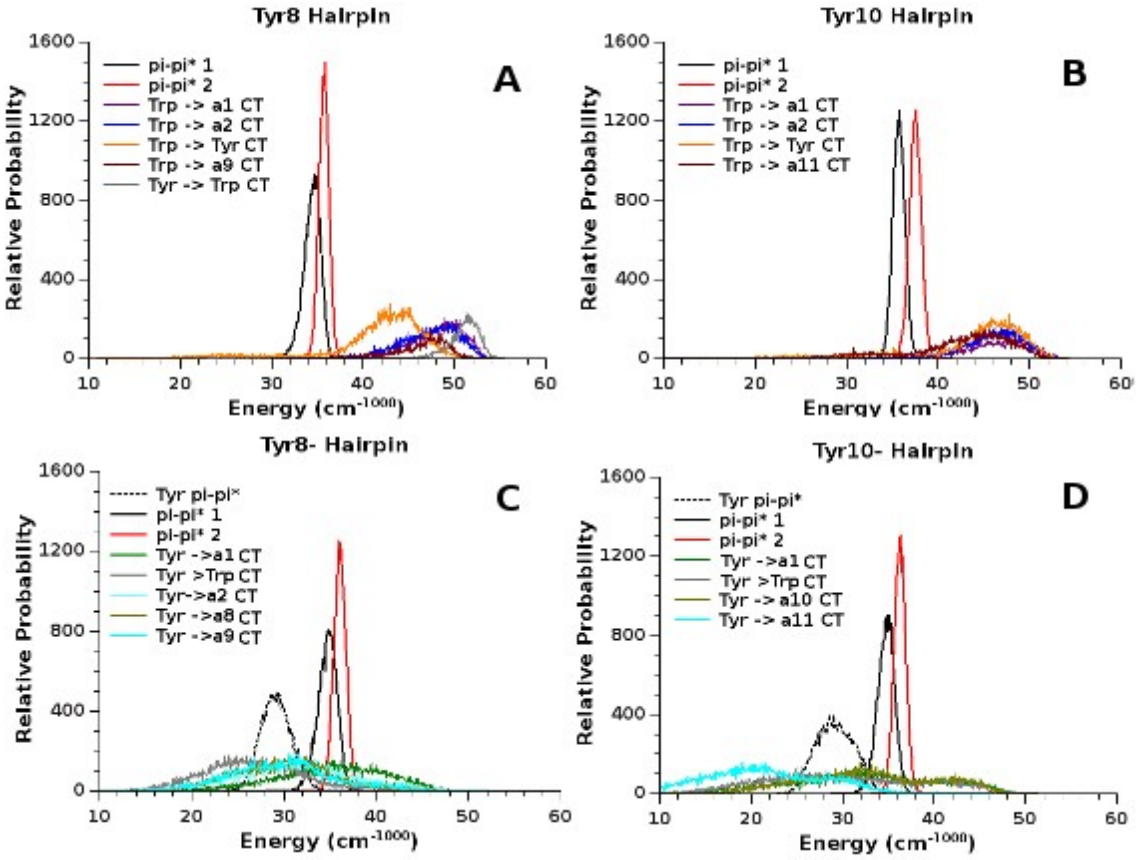

Figure 26: Tyr Hairpin Energy Distributions Distribution of π–π* and 4 lowest energy charge transfer energies of combined 20 simulations of Tyr8 (A and C) and Tyr10 (B and D). The top panels show simulations of neutral tyrosine; bottom, ionized tyrosine. Charge transfer involving amides designated as in figure 20, charge transfer involving side chains uses amino acid abbreviations.

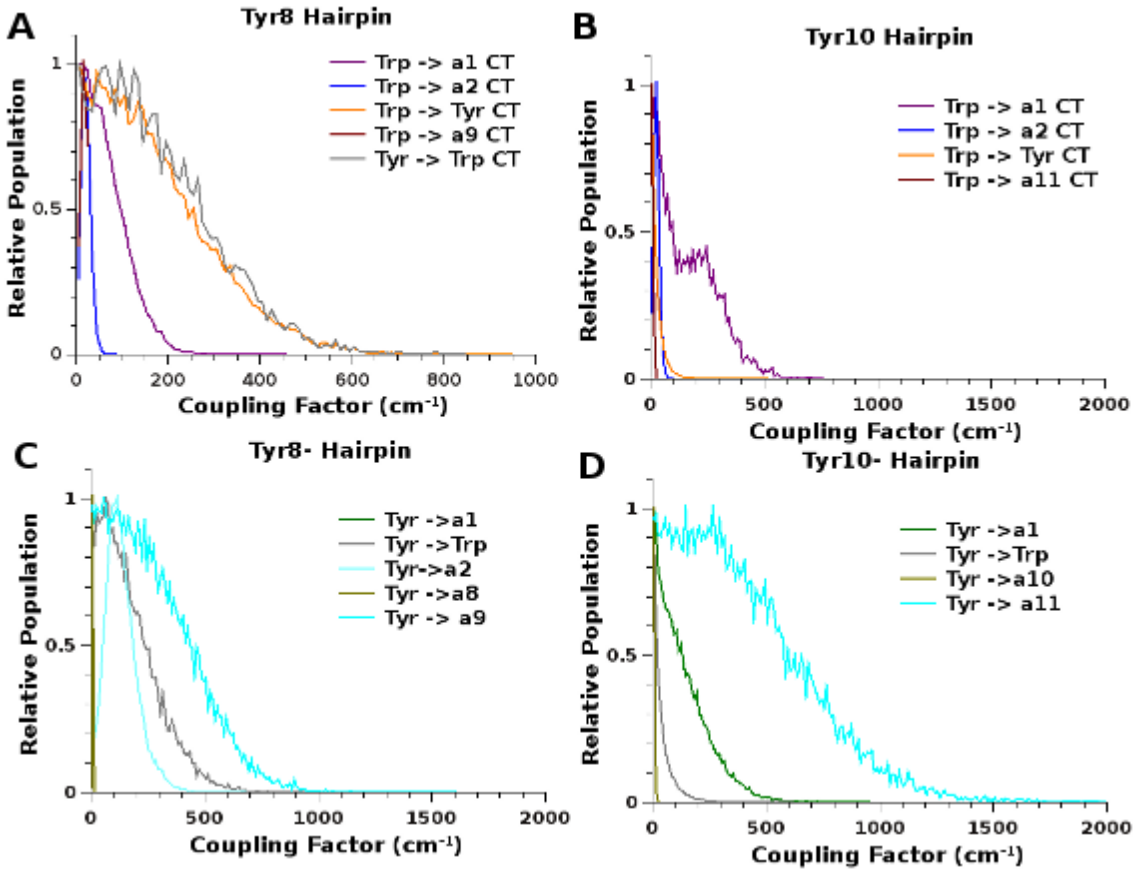

Figure 27:Tyr Hairpin Coupling Matrix Elements: Curves for various states are colored as in figure 26, and normalized as in figure 21

Figure 28 shows calculated distributions of energies of π–π* and CT states of the Trp-cage peptides. In all cases, the energies of electron transfer from the indole to the amide groups of Trp6 are markedly bimodal. Transfer to the amide on the carboxyl side of Trp6 is strongly favorable in both arms of the distribution, and transfer to the amide on the amino side is favorable in one arm. Transfer to the amide that contains the carbonyl O of Arg 16, which is hydrogen-bonded to the indole N of Trp 6, tends to be less favorable than transfer to either of these amides.

All of the Trp-cage peptides had very similar coupling matrix elements (figure 29). Transfer to a6 was very weak, with a matrix element generally less than 10 cm^{-1}. Electron transfer to a17 was somewhat more strongly coupled, with coupling factors distributed over ~300 cm^{-1} with a broad flat peak from zero to ~100 cm^{-1}. However, this state is unlikely to contribute significantly to fluorescence quenching because it is ~10000 cm^{-1} above the first π–π* transition. Instead the low energy Trp to a2 electron transfer will be helped by a strong coupling factor with a broad distribution centered at 1000 cm^{-1} and ranging from 500 cm^{-1} to 1500 cm^{-1}.

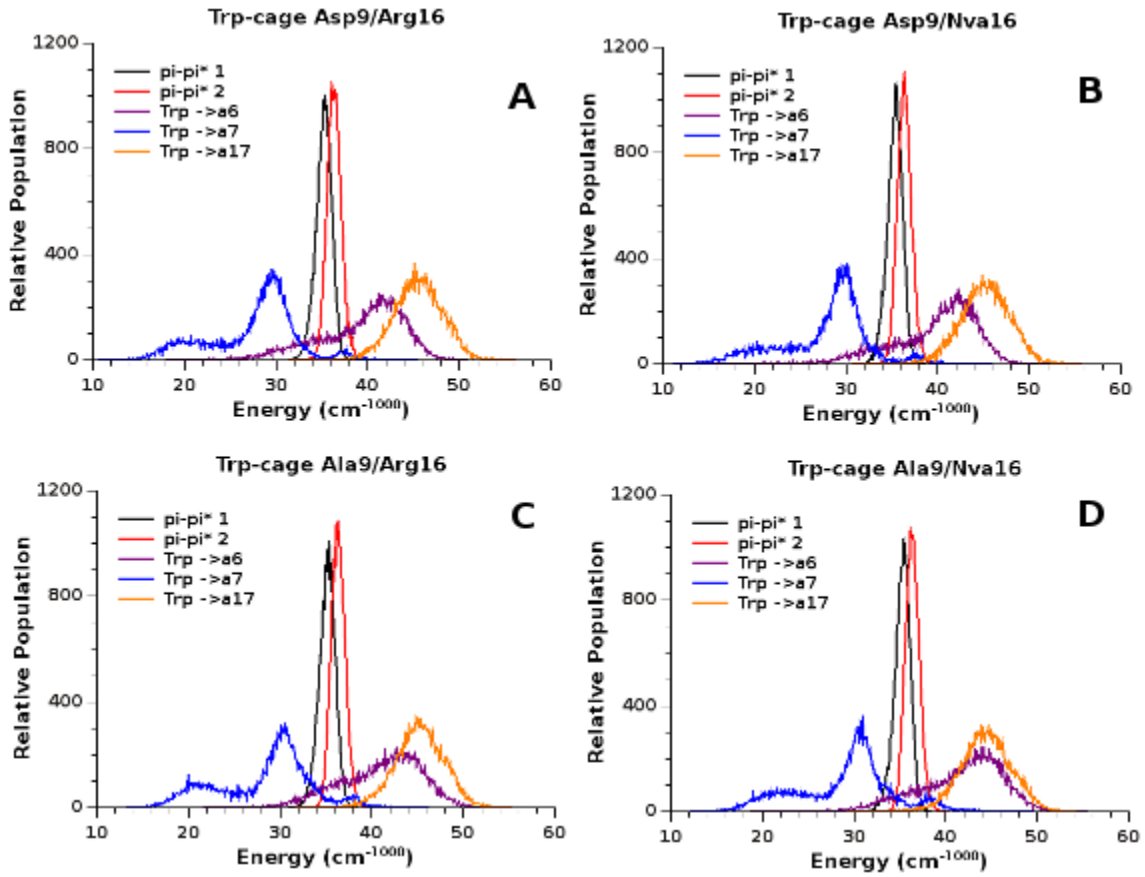

Figure 28: Trp-cage Energy Distributions Distribution of π–π* and charge transfer energies of combined 20 simulations of Wildtype Trp-cage (A) Asp9Ala (D) Arg16Nva (C) Asp9Ala/Arg16Nva (D)Trp-cage peptides. D9L, R16Ile and D9L/R16Ile had similar distributions (not shown). Other types of charge transfer did not occur in the first 16 excited states with any significant frequency. Charge transfer involving amides designated as in figure 20.

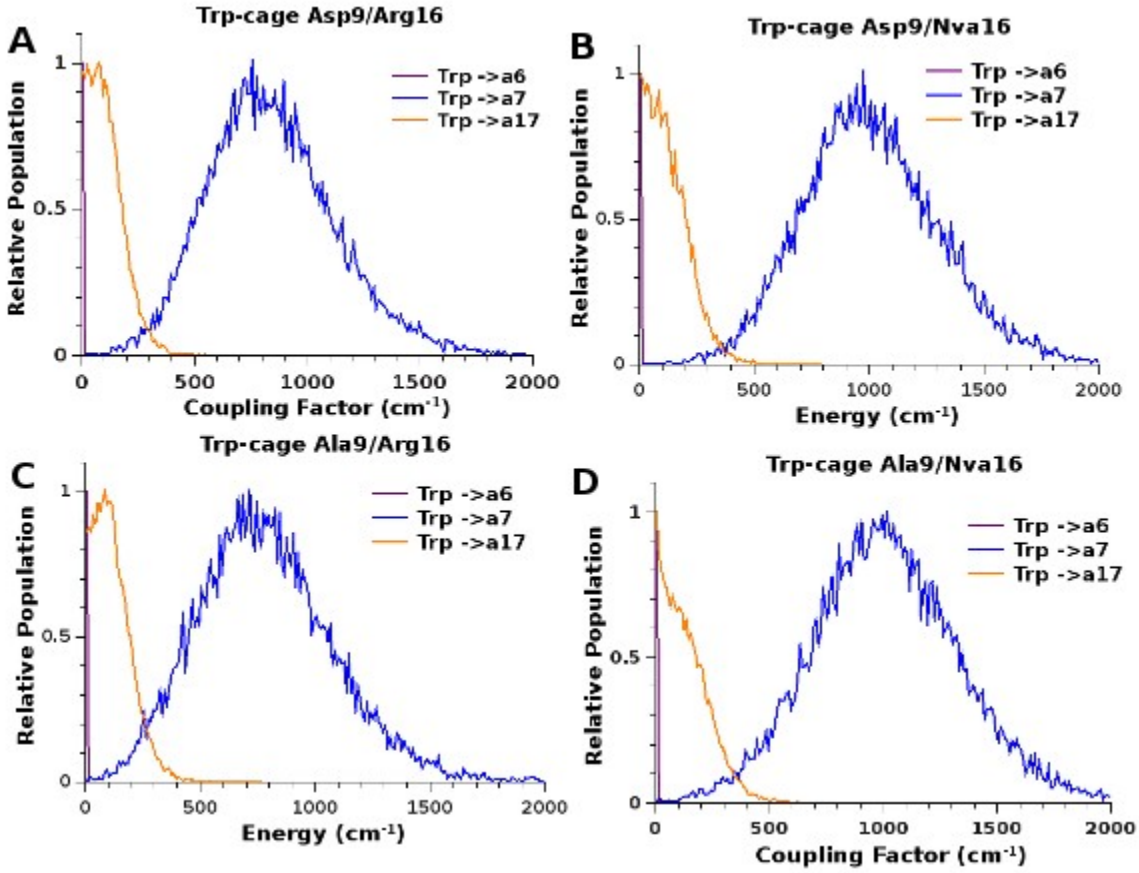

Figure 29: Trp-cage Coupling Matrix Elements: Curves for various states are colored as in figure 28, and normalized as in figure 21

Figure 30 examines how the quantum mechanical excitation energy of the charge-transfer state with the lowest average energy correlates with the classical Coulombic interaction energies of the charge donors and acceptors with water and other parts of the system. Interestingly, there is a fairly consistent correlation of the fluctuations in charge-transfer energy with the interaction between the waters and the electron acceptor (figure 30B). The slope of this correlation is similar for multiple peptides with different acceptors, and is only shifted upward for the positively charged histidine. The charge-transfer energy also shows a correlation with the interactions of the donor group with water, though this is more variable between different peptides (figure 30A). In the Trp-cage peptide, the charge-transfer energy also is correlated with the interaction of the acceptor group with other parts of the peptide that are not treated quantum mechanically (figure 30D). The interaction between the electron donor and acceptor showed only small fluctuations and were not correlated with the total charge-transfer energies (figure 30E).

To identify parts of the system that contribute to these fluctuations I examined structures that had near the average energy for the lowest charge-transfer state and determined which amino acid residues and water molecules had the greatest influence on the interaction enegies. Figures 31A and C shows the His8 hairpin as an example of the types of interactions that were seen in hairpins. The strongest interactions in the hairpin peptides, both favorable and unfavorable, tended to be with water molecules. Favorable interactions with water often involved a water molecule oriented with its oxygen near the charge donor, or with a hydrogen oriented toward the charge acceptor. In the hairpin structure shown, several waters have strongly unfavorable interactions with the reduced histidine sidechain. These are oriented with the oxygen towards histidine, which would be more favorable for the positively charged histidine prior to accepting

an electron.

Figure 31B and D show the Asp9/Arg16 Trp-cage. The reduced amide in this structure had a favorable interaction with a water molecule; however it also was strongly stabilized by interactions with Ala8, Ala10 and Gly11. While waters could move away from the electron donor or acceptor, reflecting the correlation with energy fluctuations seen in figure 30, these amino acids would be consistently in close contact with this amide, making charge transfer favorable throughout the course of the trajectories. These interactions are strong enough to favor charge transfer, despite less favorable interactions of the oxidized Trp6 with several other amino acids on the face away from the electron-accepting amide.

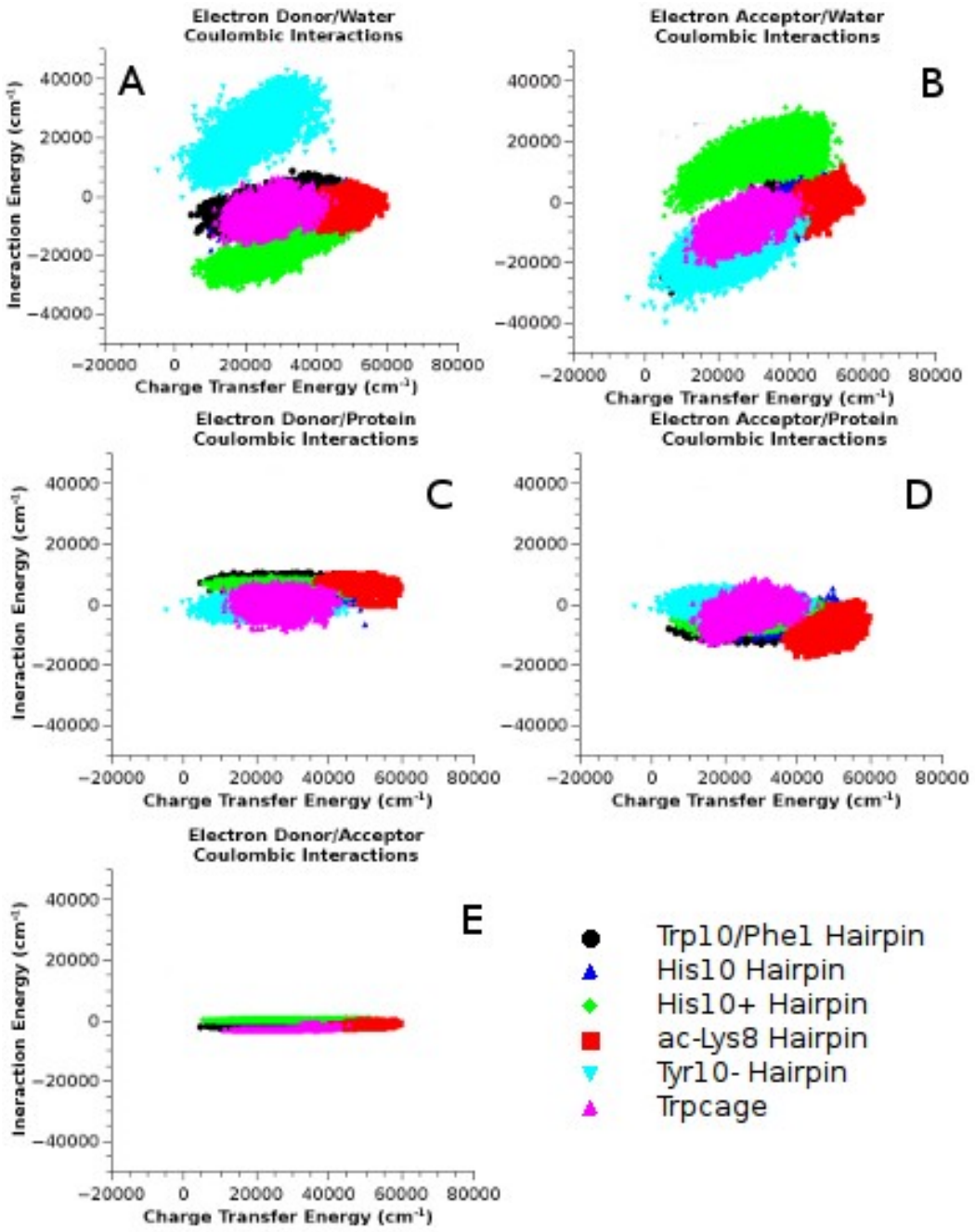

Figure 30: Examples of the correlation of charge transfer energies with Coulombic interaction energies (A,B) Interaction of the between charge donor or acceptor and other waters. (C,D) Interactions with the rest of the peptide. (E) Interactions between the donor and acceptor. In all cases the charge transfer state with the lowest average energy is shown. His10 and His10+ refer to His10 in its neutral and protonated states. Tyr10- refers to simulations with Tyr10 ionized.

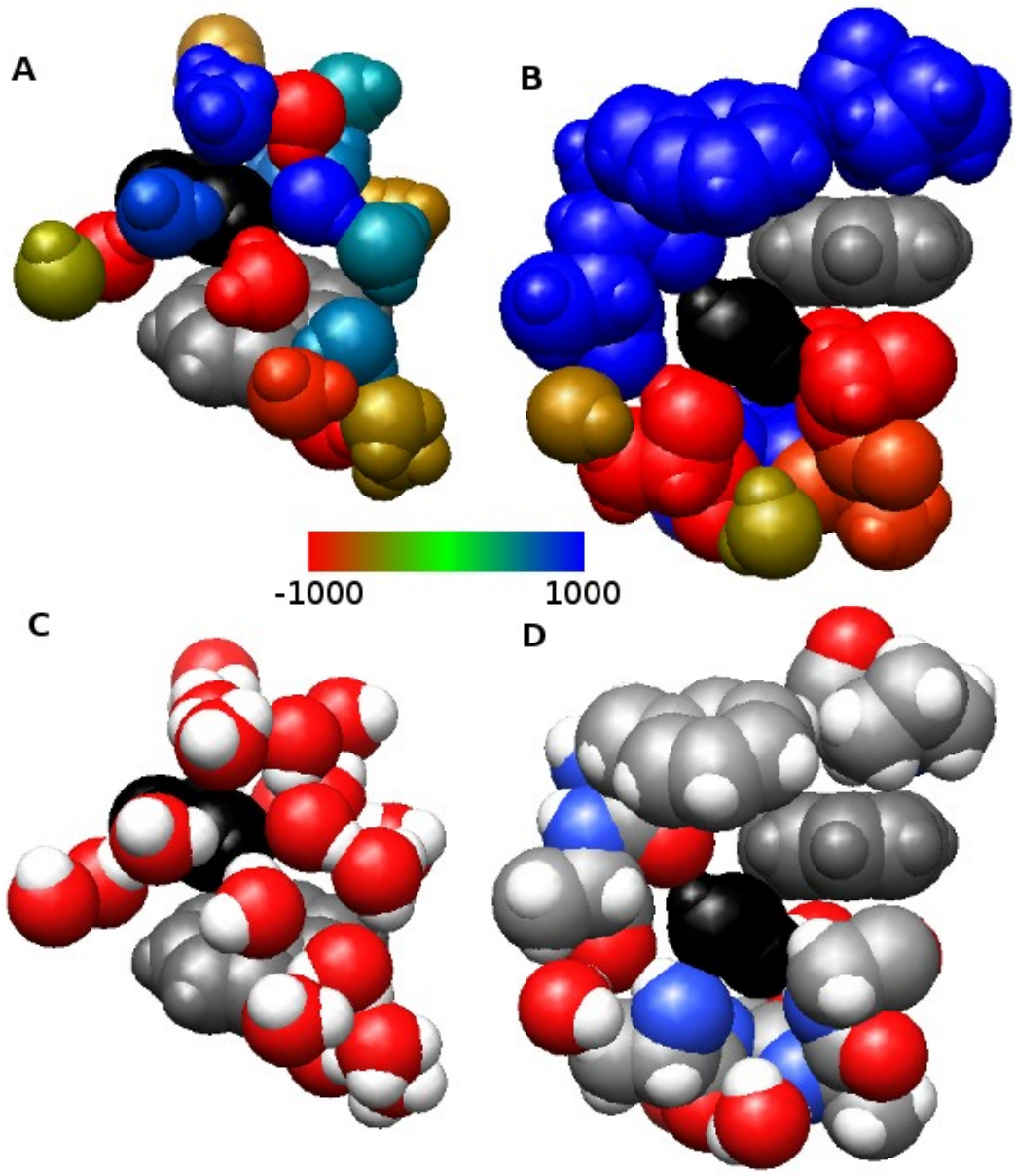

Figure 31: Molecules or amino acids that stabilize charge transfer Tryptophan is colored grey and the lowest energy charge acceptor black. Waters and other amino acids are shown if they stabilize or destabilize the charge transfer state by an energy of |500| cm^{-1} or more. A and C show the His8 hairpin; B and D, the Asp9/Arg16 Trp-cage. The structural snapshots were taken at a time when the energy of the lowest charge-transfer state was near its average value. In A and B residues are colored on a scale reflecting the contribution to the energy of the lowest charge-transfer state (red , favorable, blue, unfavorable). C and D show the same structures colored by atom type (red = oxygen, blue = nitrogen, grey = carbon, white = hydrogen).

Chapter 5: Conclusions

Quantum Yield

Qualitatively the calculations reproduce many of the variations of quantum yield that evidently reflect electron transfer. The correlation with experiment is less strong quantitatively (figure 32A), though comparable to results produced by Callis and co-workers.[42,61,63] Except for the His10 hairpin peptide, the calculations seem to overestimate intermediate levels of quenching, and do not discriminate these peptides from other more highly quenched peptides. Even unquenched peptides have underestimated quantum yields with lower values of ζ. I may also be overestimating the accessibility of very low energy states through their higher energy vibrational levels. Modifying equation 24 to include a factor to decrease the probability at large negative energy differences could take this into account. More sophisticated models of electron transfer may also produce further improvements. The calculation of coupling factors only considered the highest occupied and lowest unoccupied molecular orbitals of the donor and acceptor. Including additional orbitals could give a better model of these factors, though initial work with this approach shows only modest improvements. Equation 24 also assumes that different forms of electron transfer reactions in the same molecule are independent. Quantum mechanical interference between these reactions could decrease the amount of quenching. Accounting for this could be especially important if this treatment were to be extended to more complicated systems that involve more electron acceptors.

In spite of limited accuracy of predicted quantum yields, it is important to note that they were generated using energies directly from the quantum calculations. This contrasts with the treatment used by Callis and co-workers, which required substantial *ad hoc* shifts of the

calculated energies relative to the π–π* state.[42,61,63] Tusell and Callis' treatment of histidine in the villin headpiece[42] additionally used a different, much larger shift for electron transfer to histidine than for transfer to backbone amides, whereas I treated all forms of electron transfer the same.

A similar orientation of tryptophan relative to the quenching backbone amide is seen in both the Trp-cages and the reversed Trp/Phe hairpin. In contrast tryptophan is points away from the backbone amides in the hairpins that are not quenched by transfer to the backbone. This orientation positions sidechains from residues 8 and 10 similarly relative to the indole ring, making these favorable electron acceptors or donors in the peptides containing ionized His or Tyr and neutral Asp and Glu. This suggests quenching may depend to some extent on the orientation of the indole ring relative to a potential electron donor or acceptor.

Callis et al.[63] saw no correlation between the tryptophan torsion angle and quantum yield for a variety of proteins. They did however, see a correlation with the coupling constant for electron transfer and did not look for correlations with the orientation of quencher other than the tryptophan backbone. While my calculations showed that strong coupling to a charge transfer state was not necessarily associated with favorable quenching, for example in the case for Asn8 and Gln8 hairpins, a quenching state tended to also have strong coupling, the exceptions being Glu8 and His10. The weaker coupling of Glu8 seems consistent with the fact that this peptide is slightly less quenched compared to Asp8, which has a charge-transfer state with both strong coupling and low energy. The weak coupling for His10 appears more anomalous. This peptide is the most prominent outlier from the correlation between the calculated and measured quantum yields.

Most of the electron transfer I observed had been described by others,[42,58,61,63] though comparison of amide and sidechain quenching had been rudimentary until recently.[42] However charge transfer involving reduction of tryptophan appears to be novel. Excitation of tryptophan would leave a hole in the HOMO, which could be filled by oxidation of a tyrosine anion, providing one path by which electron transfer from tyrosine could quench tryptophan fluorescence. Oxidation of tyrosine could also occur through exciton states that contain contributions from both tryptophan and tyrosine. Tyrosine radicals have been detected in a variety of proteins, including ribonucleotide reductases,[99,100] photosystem II,[101,102] cytochrome *c* oxidase,[103] galactose oxidase,[104,105] prostaglandin synthase [106–108] and cytochrome P450cam.[109]

Analysis of the proton transfer dependent quenching is more difficult, as these reactions are not as easily integrated into mixed MD/QM calculations. The large difference of the quantum yields of Orn8 and Lys8 hairpins suggest that there may be stonger geometric considerations for proton transfer. There may also be some significance in the difference between the weak quenching of Tyr8 and Tyr10 and the stronger quenching Chen and Barkley described.[58] Chen and Barkly studied quenching of 3MI in solution which would not have required a specific orientation. A stricter dependence on a specific orientation for proton transfer would fit with observations that photochemical proton transfer to tryptophan results in deuterium exchange at specific carbon atoms.[60,110] However the MD simulations of the hairpin peptides do not explain why ornithine showed strong quenching while lysine did not, since lysine was nearer to the positions in the indole ring where proton exchange would be expected. This may reflect the lack of counterion, or more subtle quantum mechanical effects than can currently be treated with ENZYQ.

Emission Energy

The simulations of the tryptophan peptides all overestimate both the emission and absorption energies. There also is little or no correlation with observed emission and the calculated energy (figure 32B). This was not unexpected since the absorption and emission energies of 3MI in solution also were overestimated. It would be difficult to accurately predict energies the small differences in the emission energies of the peptides that were studied, though the calculations show even less variation than the measured energies.

In hindsight the narrow range of emission energies is not surprising. Despite the variety of amino acids that were substituted, the general scaffold remained constant within each of the two sets of peptides. Larger shifts in energy could require more drastic changes in the tryptophan environment. In particular the location of tryptophan in the hairpin system is not well suited to changing the electric field parallel to the long axis of the indole ring, which would be needed to produce a large Stark effect.[50] The Trp-cage peptides might have been expected to show a larger range of emission energies, because two charged groups near the end of the indole ring were changed. In fact, mutating these residues did have more effect than was seen in the hairpins. The relatively large blue-shift in the D9A mutant would be consistent with internal Stark effects. However similar blue shifting did not occur in the D9L mutant, possibly reflecting different orientations of the positively charged Arg16. Unfortunately the specific orientation of arginine is difficult to determine by NMR in these peptides. Shifts of the emission to longer wavelengths was observed in Arg16 mutants; however, these shifts could instead be attributed to partial unfolding, which would also be expected to result in a red-shift. This is especially a factor in the Arg16Nva mutant which was made in the less stable Trp-cage 10b system.

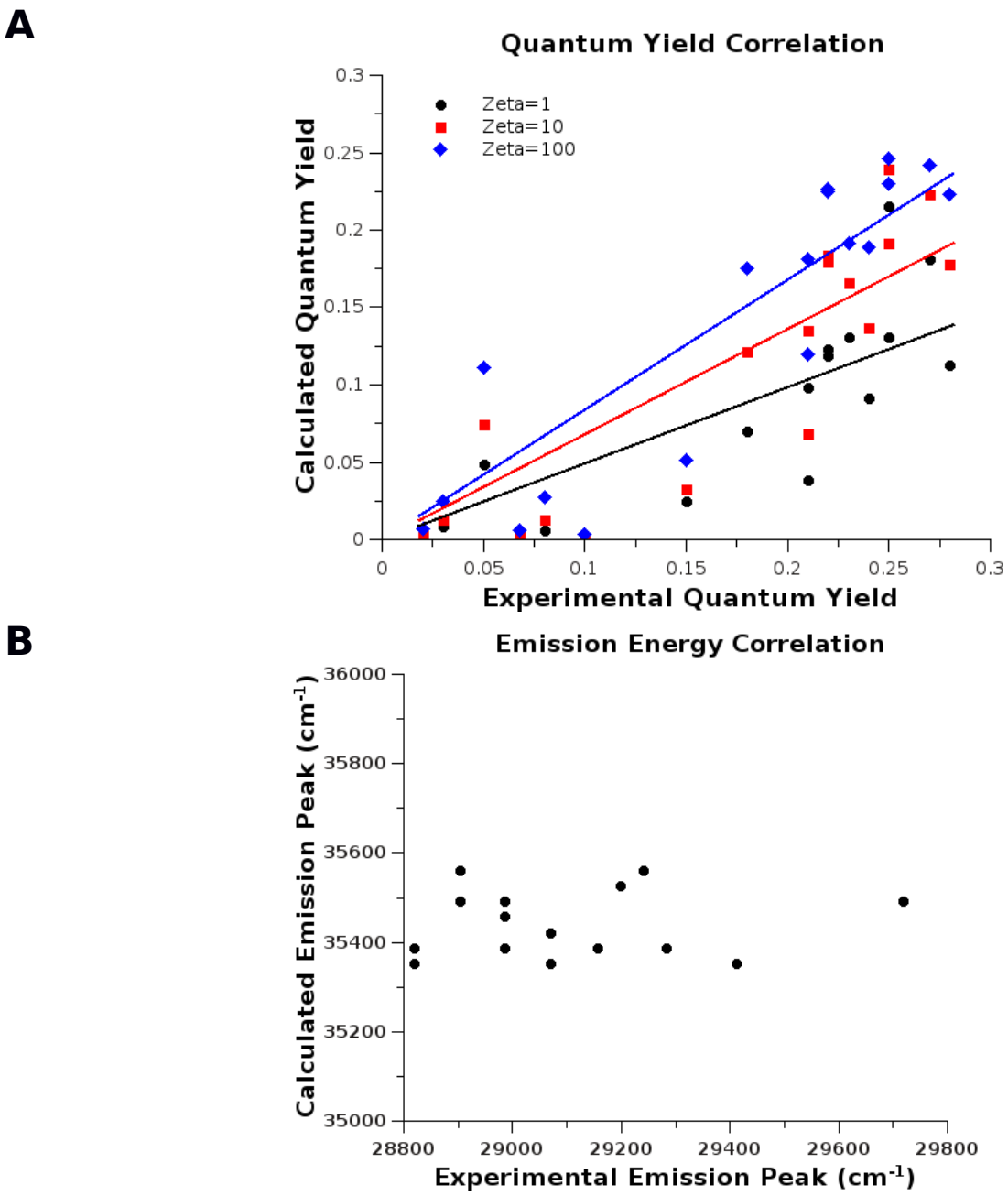

Figure 32: Correlation Between Calculated and Measured Properties (A) Correlation of the measured fluorescence yield with the calculated quantity 0.2475x(1-*f*), where *f* is the time-averaged probability of quenching (see equation 24 and 25) with three values of ζ. Lines show linear fit that passes through the origin. (B) Correlation of the measured peak emission wavelength with the calculated peak from a Boltzmann weighted histogram of the first two π–π* states.

REFERENCES

(1) Ulmanen, I.; Peränen, J.; Tenhunen, J.; Tilgmann, C.; Karhunen, T.; Panula, P.; Bernasconi, L.; Aubry, J.-P.; Lundström, K. *European Journal of Biochemistry* **1997**, *243*, 452–459.

(2) Lotta, T.; Vidgren, J.; Tilgmann, C.; Ulmanen, I.; Melen, K.; Julkunen, I.; Taskinen, J. *Biochemistry* **1995**, *34*, 4202–4210.

(3) ØVERBYE, A.; Seglen, P. O. *Biochemical Journal* **2009**, *417*, 535–545.

(4) Barnnett, J.; Heron, J.; Ring, S. M.; Golding, J.; Goldman, D.; Xu, K.; Jones, P. B. *The American Journal of Psychiatry* **2007**, *164*, 142–149.

(5) Williams, H. J.; Owen, M. J.; O'Donovan, M. C. *Schizophrenia Bulletin* **2007**, *33*, 635 –641.

(6) Dickerson, F. B.; Boronow, J. J.; Stallings, C.; Origoni, A. E.; Sullens, A.; Yolken, R. H. *Schizophrenia Research* **2007**, *96*, 87–92.

(7) Illi, A.; Kampman, O.; Hänninen, K.; Anttila, S.; Mattila, K. M.; Katila, H.; Rontu, R.; Hurme, M.; Lehtimäki, T.; Leinonen, E. *Hum. Psychopharmacol. Clin. Exp.* **2007**, *22*, 211–215.

(8) Strous, R. D.; Ritsner, M. S.; Adler, S.; Ratner, Y.; Maayan, R.; Kotler, M.; Lachman, H.; Weizman, A. *European Neuropsychopharmacology* **2009**, *19*, 14–22.

(9) Dickerson, F. B.; Boronow, J. J.; Stallings, C.; Origoni, A. E.; Cole, S.; Leister, F.; Krivogorsky, B.; Yolken, R. H. *Bipolar Disorders* **2006**, *8*, 124–132.

(10) Karayiorgou, M.; Sobin, C.; Blundell, M. L.; Galke, B. L.; Malinova, L.; Goldberg, P.; Ott, J.; Gogos, J. A. *Biological Psychiatry* **1999**, *45*, 1178–1189.

(11) Kauhanen, J.; Hallikainen, T.; Tuomainen, T.-P.; Koulu, M.; Karvonen, M. K.; Salonen, J. T.; Tiihonen, J. *Alcoholism: Clinical and Experimental Research* **2000**, *24*, 135–139.

(12) Retz, W.; Rösler, M.; Kissling, C.; Wiemann, S.; Hünnerkopf, R.; Coogan, A.; Thome, J.; Freitag, C. *Journal of Neural Transmission* **2008**, *115*, 323–329.

(13) Williams-Gray, C. H.; Hampshire, A.; Barker, R. A.; Owen, A. M. *Brain* **2008**, *131*, 397 –408.

(14) Truong, D. D. *Clin Interv Aging* **2009**, *4*, 109–113.

(15) Dreher, J.-C.; Kohn, P.; Kolachana, B.; Weinberger, D. R.; Berman, K. F. *Proceedings of the National Academy of Sciences* **2009**, *106*, 617 –622.

(16) Schmack, K.; Schlagenhauf, F.; Sterzer, P.; Wrase, J.; Beck, A.; Dembler, T.; Kalus, P.; Puls, I.; Sander, T.; Heinz, A.; Gallinat, J. *NeuroImage* **2008**, *42*, 1631–1638.

(17) Tan, H.-Y.; Chen, Q.; Goldberg, T. E.; Mattay, V. S.; Meyer-Lindenberg, A.; Weinberger, D. R.; Callicott, J. H. *The Journal of Neuroscience* **2007**, *27*, 13393 –13401.

(18) Weickert, T. W.; Goldberg, T. E.; Mishara, A.; Apud, J. A.; Kolachana, B. S.; Egan, M. F.; Weinberger, D. R. *Biological Psychiatry* **2004**, *56*, 677–682.

(19) Bilder, R. M.; Volavka, J.; Czobor, P. á.; Malhotra, A. K.; Kennedy, J. L.; Ni, X.; Goldman, R. S.; Hoptman, M. J.; Sheitman, B.; Lindenmayer, J.-P.; Citrome, L.; McEvoy, J. P.; Kunz, M.; Chakos, M.; Cooper, T. B.; Lieberman, J. A. *Biological Psychiatry* **2002**, *52*, 701–707.

(20) Papaleo, F.; Crawley, J. N.; Song, J.; Lipska, B. K.; Pickel, J.; Weinberger, D. R.; Chen, J. *The Journal of Neuroscience* **2008**, *28*, 8709 –8723.

(21) Kambur, O.; Talka, R.; Ansah, O.; Kontinen, V.; Pertovaara, A.; Kalso, E.; Männistö, P. *British Journal of Pharmacology* **2010**, *161*, 1553–1565.

(22) Roussos, P.; Giakoumaki, S. G.; Rogdaki, M.; Pavlakis, S.; Frangou, S.; Bitsios, P. *Psychological Medicine* **2008**, *38*, 1651–1658.

(23) Cerasa, A.; Gioia, M. C.; Labate, A.; Liguori, M.; Lanza, P.; Quattrone, A. *NeuroReport* **2008**, *19*, 405–408 10.1097/WNR.0b013e3282f5f784.

(24) Rutherford, K.; Le Trong, I.; Stenkamp, R. E.; Parson, W. W. *Journal of Molecular Biology* **2008**, *380*, 120–130.
(25) Nackley, A. G.; Shabalina, S. A.; Tchivileva, I. E.; Satterfield, K.; Korchynskyi, O.; Makarov, S. S.; Maixner, W.; Diatchenko, L. *Science* **2006**, *314*, 1930 –1933.
(26) Rutherford, K.; Alphandéry, E.; McMillan, A.; Daggett, V.; Parson, W. W. *Biochimica et Biophysica Acta (BBA) - Proteins & Proteomics* **2008**, *1784*, 1098–1105.
(27) Rutherford, K.; Bennion, B. J.; Parson, W. W.; Daggett, V. *Biochemistry* **2006**, *45*, 2178–2188.
(28) Tsuji, E.; Okazaki, K.; Isaji, M.; Takeda, K. *Journal of Structural Biology* **2009**, *165*, 133–139.
(29) Szabo, A. G.; Rayner, D. M. *J. Am. Chem. Soc.* **1980**, *102*, 554–563.
(30) Eftink, M. R.; Jia, J.; Hu, D.; Ghiron, C. A. *J. Phys. Chem.* **1995**, *99*, 5713–5723.
(31) Bai, H.-W.; Shim, J.-Y.; Yu, J.; Zhu, B. T. *Chem. Res. Toxicol.* **2007**, *20*, 1409–1425.
(32) Shield, A. J.; Thomae, B. A.; Eckloff, B. W.; Wieben, E. D.; Weinshilboum, R. M. *Mol Psychiatry 9*, 151–160.
(33) Kozachkov, L.; Padan, E. *Proceedings of the National Academy of Sciences* **2011**, *108*, 15769 –15774.
(34) Gaines, W. A.; Sehorn, M. G.; Marcotte, W. R. *Journal of Biological Chemistry* **2010**, *285*, 40745 –40753.
(35) Chen, Y.; Erickson, H. P. *Biochemistry* **2011**, *50*, 4675–4684.
(36) Woo, H.-J.; Jiang, J.; Lafer, E. M.; Sousa, R. *Biochemistry* **2009**, *48*, 11470–11477.
(37) Katz, A.; Alimova, A.; Futerman, E.; Katz, G.; Wei, H.; Gottlieb, P. *Photochemistry and Photobiology* **2011**, no.
(38) James, N. G.; Byrne, S. L.; Steere, A. N.; Smith, V. C.; MacGillivray, R. T. A.; Mason, A. B. *Biochemistry* **2009**, *48*, 2858–2867.
(39) Christie, J. M.; Arvai, A. S.; Baxter, K. J.; Heilmann, M.; Pratt, A. J.; O'Hara, A.; Kelly, S. M.; Hothorn, M.; Smith, B. O.; Hitomi, K.; Jenkins, G. I.; Getzoff, E. D. *Science* **2012**, *335*, 1492 –1496.
(40) Jas, G. S.; Eaton, W. A.; Hofrichter, J. *J. Phys. Chem. B* **2000**, *105*, 261–272.
(41) Thompson, P. A.; Muñoz, V.; Jas, G. S.; Henry, E. R.; Eaton, W. A.; Hofrichter, J. *J. Phys. Chem. B* **1999**, *104*, 378–389.
(42) Tusell, J. R.; Callis, P. R. *J. Phys. Chem. B* **2012**.
(43) Kubelka, J.; Eaton, W. A.; Hofrichter, J. *Journal of Molecular Biology* **2003**, *329*, 625–630.
(44) Gong, H.; Murphy, P. W.; Langille, G. M.; Minielly, S. J.; Murphy, A.; McMaster, C. R.; Byers, D. M. *Biochimica et Biophysica Acta (BBA) - Proteins & Proteomics* **2008**, *1784*, 1835–1843.
(45) Kosinski-Collins, M. S.; Flaugh, S. L.; King, J. *Protein Science* **2004**, *13*, 2223–2235.
(46) Bloemendal, H.; de Jong, W.; Jaenicke, R.; Lubsen, N. H.; Slingsby, C.; Tardieu, A. *Progress in Biophysics and Molecular Biology* **2004**, *86*, 407–485.
(47) Xu, J.; Chen, J.; Toptygin, D.; Tcherkasskaya, O.; Callis, P.; King, J.; Brand, L.; Knutson, J. R. *J. Am. Chem. Soc.* **2009**, *131*, 16751–16757.
(48) Chen, J.; Flaugh, S. L.; Callis, P. R.; King, J. *Biochemistry* **2006**, *45*, 11552–11563.
(49) Callis, P. R.; Burgess, B. K. *J. Phys. Chem. B* **1997**, *101*, 9429–9432.
(50) Vivian, J. T.; Callis, P. R. *Biophysical Journal* **2001**, *80*, 2093–2109.
(51) Broos, J.; Tveen-Jensen, K.; de Waal, E.; Hesp, B. H.; Jackson, J. B.; Canters, G. W.; Callis, P. R. *Angewandte Chemie International Edition* **2007**, *46*, 5137–5139.
(52) Toptygin, D.; Woolf, T. B.; Brand, L. *J. Phys. Chem. B* **2010**, *114*, 11323–11337.
(53) Pan, C.-P.; Muiño, P. L.; Barkley, M. D.; Callis, P. R. *J. Phys. Chem. B* **2011**, *115*, 3245–3253.
(54) COWGILL, R. *Arch Biochem Biophys* **1963**, *100*, 36–44.
(55) Shinttzky, M.; Goldman, R. *European Journal of Biochemistry* **1967**, *3*, 139–144.
(56) Steiner, R. F.; Kirby, E. P. *J. Phys. Chem.* **1969**, *73*, 4130–4135.
(57) Ricci, R. W.; Nesta, J. M. *J. Phys. Chem.* **1976**, *80*, 974–980.
(58) Chen, Y.; Barkley, M. D. *Biochemistry* **1998**, *37*, 9976–9982.
(59) Qiu, W.; Li, T.; Zhang, L.; Yang, Y.; Kao, Y.-T.; Wang, L.; Zhong, D. *Chemical Physics* **2008**, *350*, 154–164.

(60) Yu, H. T.; Colucci, W. J.; McLaughlin, M. L.; Barkley, M. D. *J. Am. Chem. Soc.* **1992**, *114*, 8449–8454.
(61) Callis, P. R.; Liu, T. *The Journal of Physical Chemistry B* **2004**, *108*, 4248–4259.
(62) Pan, C.-P.; Callis, P. R.; Barkley, M. D. *J. Phys. Chem. B* **2006**, *110*, 7009–7016.
(63) Callis, P. R.; Petrenko, A.; Muiño, P. L.; Tusell, J. R. *J. Phys. Chem. B* **2007**, *111*, 10335–10339.
(64) Warshel, A.; Sharma, P. K.; Kato, M.; Parson, W. W. *Biochimica et Biophysica Acta (BBA) - Proteins & Proteomics* **2006**, *1764*, 1647–1676.
(65) Parson, W. W.; Warshel, A. In *Biophysical Techniques in Photosynthesis*; Springer, 2008; pp. 401–420.
(66) Eidenschink, L.; Kier, B. L.; Huggins, K. N. L.; Andersen, N. H. *Proteins* **2009**, *75*, 308–322.
(67) Kier, B. L.; Andersen, N. H. *J. Am. Chem. Soc.* **2008**, *130*, 14675–14683.
(68) Kier, B. L.; Shu, I.; Eidenschink, L. A.; Andersen, N. H. *Proc. Natl. Acad. Sci. USA* **2010**, *107*, 10466–10471.
(69) Williams, D. V.; Barua, B.; Andersen, N. H. *Org. Biomol. Chem.* **2008**, *6*, 4287–4289.
(70) Barua, B.; Lin, J. C.; Williams, V. D.; Kummler, P.; Neidigh, J. W.; Andersen, N. H. *Protein Engineering Design and Selection* **2008**, *21*, 171–185.
(71) McMillan, A. W.; Kier, B. L.; Shu, I.; Byrne, A.; Andersen, N.; Parson, W. W. *Manuscript in Preparation* **2012**.
(72) Lee, F. S.; Chu, Z. T.; Warshel, A. *Journal of Computational Chemistry* **1993**, *14*, 161–185.
(73) Warshel, A.; Karplus, M. *J. Am. Chem. Soc.* **1972**, *94*, 5612–5625.
(74) Warshel, A.; Lappicirella, A. *J. Am. Chem. Soc.* **1981**, *103*, 4664–4673.
(75) King, G.; Warshel, A. *The Journal of Chemical Physics* **1989**, *91*, 3647–3661.
(76) Lee, F. S.; Warshel, A. *J. Chem. Phys.* **1992**, *97*, 3100–3107.
(77) Takigawa, T.; Ashida, T.; Sasada, Y.; Kakudo, M. *Bulletin of the Chemical Society of Japan* **1966**, *39*, 2369–2378.
(78) Callis, P. R.; Vivian, J. T.; Slater, L. S. *Chemical Physics Letters* **1995**, *244*, 53–58.
(79) Del Re, G. *Thor. Chim Acta* **1958**, *1*, 4031–4040.
(80) Alden, R. G.; Johnson, E.; Nagarajan, V.; Parson, W. W.; Law, C. J.; Cogdell, R. G. *The Journal of Physical Chemistry B* **1997**, *101*, 4667–4680.
(81) Moser, C. C.; Dutton, P. L. *Biochimica et Biophysica Acta (BBA) - Bioenergetics* **1992**, *1101*, 171–176.
(82) Westbrook, J. D.; Levy, R. M.; Krogh-Jespersen, K. *Proc. SPIE* **1992**, *1640*, 10–19.
(83) Thole, B. T. *Chemical Physics* **1981**, *59*, 341–350.
(84) van Duijnen, P. T.; Swart, M. *The Journal of Physical Chemistry A* **1998**, *102*, 2399–2407.
(85) Bernardo, D. N.; Ding, Y.; Krogh-Jespersen, K.; Levy, R. M. *J. Phys. Chem.* **1994**, *98*, 4180–4187.
(86) Burnham, C.; Xantheas, S. *J. Chem. Phys.* **2002**, *116*, 1500–1510.
(87) Ren, P.; Ponder, J. W. *J. Phys. Chem. B* **2003**, *107*, 5933–5947.
(88) Elking, D.; Darden, T.; Woods, R. J. *J. Comput. Chem.* **2007**, *28*, 1261–1274.
(89) Marcus, R. A. *J. Chem. Phys.* **1956**, *24*, 966–978.
(90) Parson, W. W.; Warshel, A. *J. Phys. Chem. B* **2004**, *108*, 10474–10483.
(91) Parson, W. W.; Warshel, A. *Chemical Physics* **2004**, *296*, 201–216.
(92) Warshel, A.; Chu, Z. T.; Parson, W. W. *Science* **1989**, *246*, 112–116.
(93) Alden, R. G.; Parson, W. W.; Chu, Z. T.; Warshel, A. *J. Am. Chem. Soc.* **1995**, *117*, 12284–12298.
(94) Silvestrelli, P. L.; Parrinello, M. *The Journal of Chemical Physics* **1999**, *111*, 3572–3580.
(95) Soper, A. K.; Benmore, C. J. *Phys. Rev. Lett.* **2008**, *101*, 065502.
(96) Sorenson, J. M.; Hura, G.; Glaeser, R. M.; Head-Gordon, T. *J. Chem. Phys.* **2000**, *113*, 9149–9161.
(97) Ichikawa, K.; Kameda, Y.; Yamaguchi, T.; Wakita, H.; Misawa, M. *Molecular Physics* **1991**, *73*, 79–86.
(98) Lami, H.; Glasser, N. *The Journal of Chemical Physics* **1986**, *84*, 597–604.
(99) Larsson, A.; Sjoberg, B. *EMBO Journal* **1986**, *5*, 2037–2040.
(100) Reece, S. Y.; Seyedsayamdost, M. R.; Stubbe, J.; Nocera, D. G. *J. Am. Chem. Soc.* **2007**, *129*, 13828–13830.

(101) Debus, R. J.; Barry, B. A.; Babcock, G. T.; McIntosh, L. *Proceedings of the National Academy of Sciences* **1988**, *85*, 427 –430.
(102) Berthomieu, C.; Hienerwadel, R. *Biochimica et Biophysica Acta (BBA) - Bioenergetics* **2005**, *1707*, 51–66.
(103) MacMillan, F.; Kannt, A.; Behr, J.; Prisner, T.; Michel, H. *Biochemistry* **1999**, *38*, 9179–9184.
(104) Lee, Y.-K.; Whittaker, M. M.; Whittaker, J. W. *Biochemistry* **2008**, *47*, 6637–6649.
(105) Whittaker, J. W. *Archives of Biochemistry and Biophysics* **2005**, *433*, 227–239.
(106) Malkowski, M. G.; Ginell, S. L.; Smith, W. L.; Garavito, R. M. *Science* **2000**, *289*, 1933–1937.
(107) Rogge, C. E.; Ho, B.; Liu, W.; Kulmacz, R. J.; Tsai, A.-L. *Biochemistry* **2005**, *45*, 523–532.
(108) Wu, G.; Tsai, A.-L.; Kulmacz, R. J. *Biochemistry* **2009**, *48*, 11902–11911.
(109) Schünemann, V.; Lendzian, F.; Jung, C.; Contzen, J.; Barra, A.-L.; Sligar, S. G.; Trautwein, A. X. *Journal of Biological Chemistry* **2004**, *279*, 10919 –10930.
(110) Saito, I.; Sugiyama, H.; Yamamoto, A.; Muramatsu, S.; Matsuura, T. *J. Am. Chem. Soc.* **1984**, *106*, 4286–4287.Andy McMillan was born in Denver, Colorado. At the the University of Colorado he earned a Bachelor of Arts degree in Molecular, Cellular and Developmental Biology and Biochemistry. In 2012 he earned a Doctor of Philosophy at the University of Washington in Biochemistry.